Article

Cell Reports

Synapse-Selective Control of Cortical Maturation and Plasticity by Parvalbumin-Autonomous Action of SynCAM 1

Graphical Abstract

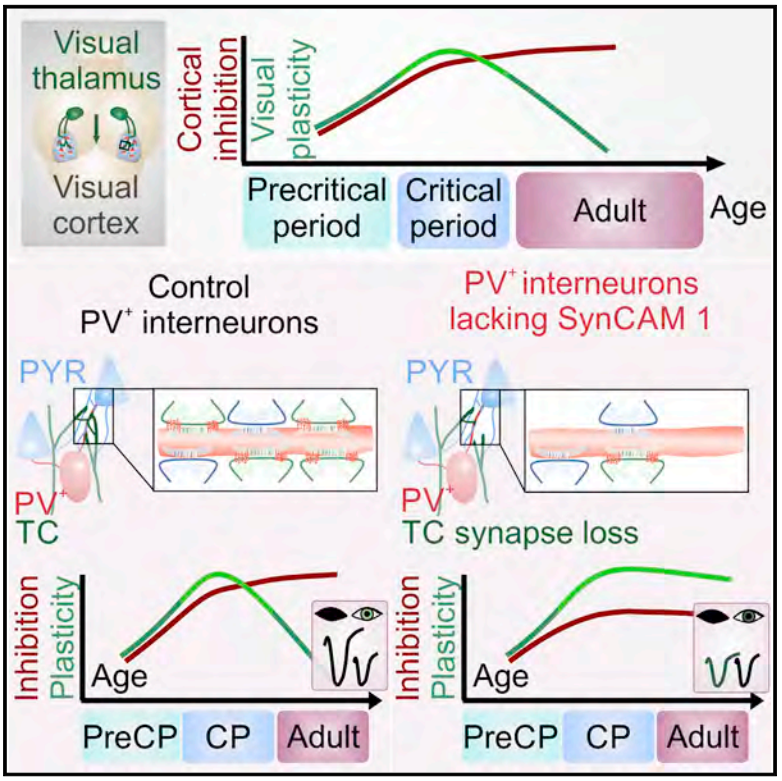

Highlights

- Visual plasticity selectively regulates SynCAM 1 expression
- SynCAM 1 controls thalamic inputs onto cortical parvalbumin (PV^+) interneurons
- PV^+-specific SynCAM 1 knockdown restores plasticity in the mature visual cortex
- Thalamic inputs on PV^+ interneurons are synaptic sites for critical period closure

Authors

Adema Ribic, Michael C. Crair, Thomas Biederer

Correspondence

adema.ribic@tufts.edu (A.R.), thomas.biederer@tufts.edu (T.B.)

In Brief

Ribic et al. show that cortical plasticity is actively restricted by the synapse-organizing molecule SynCAM 1. The protein acts in parvalbumin interneurons to recruit excitatory thalamocortical terminals. This controls the maturation of inhibition and actively limits cortical plasticity, revealing a synaptic locus for closure of cortical critical periods.

Ribic et al., 2019, Cell Reports *26*, 381–393
January 8, 2019
https://doi.org/10.1016/j.celrep.2018.12.069

CellPress

Cell Reports
Article

Synapse-Selective Control of Cortical Maturation and Plasticity by Parvalbumin-Autonomous Action of SynCAM 1

Adema Ribic,[1,*] Michael C. Crair,[2] and Thomas Biederer[1,3,*]
[1]Department of Neuroscience, Tufts University School of Medicine, Boston, MA 02111, USA
[2]Department of Neuroscience, Yale University School of Medicine, New Haven, CT 06510, USA
[3]Lead Contact
*Correspondence: adema.ribic@tufts.edu (A.R.), thomas.biederer@tufts.edu (T.B.)
https://doi.org/10.1016/j.celrep.2018.12.069

SUMMARY

Cortical plasticity peaks early in life and tapers in adulthood, as exemplified in the primary visual cortex (V1), wherein brief loss of vision in one eye reduces cortical responses to inputs from that eye during the critical period but not in adulthood. The synaptic locus of cortical plasticity and the cell-autonomous synaptic factors determining critical periods remain unclear. We here demonstrate that the immunoglobulin protein Synaptic Cell Adhesion Molecule 1 (SynCAM 1/Cadm1) is regulated by visual experience and limits V1 plasticity. Loss of SynCAM 1 selectively reduces the number of thalamocortical inputs onto parvalbumin (PV^+) interneurons, impairing the maturation of feedforward inhibition in V1. SynCAM 1 acts in PV^+ interneurons to actively restrict cortical plasticity, and brief PV^+-specific knockdown of SynCAM 1 in adult visual cortex restores juvenile-like plasticity. These results identify a synapse-specific, cell-autonomous mechanism for thalamocortical visual circuit maturation and closure of the visual critical period.

INTRODUCTION

Imbalanced visual input during the postnatal critical period for development of visual function leads to a permanent reduction in cortical responses to the affected eye and an increase in responses to the healthy eye, a phenomenon known as ocular dominance plasticity (ODP) (Espinosa and Stryker, 2012). The elevated potential for ODP during the critical period promotes the extensive sensory experience-dependent refinement of synapses during cortical development (Espinosa and Stryker, 2012; Wang et al., 2010). Plasticity tapers off as the brain matures, such that brief manipulation of visual input in adult animal models has no effect on cortical responses (Kuhlman et al., 2013).

There is considerable evidence that elevated cortical inhibitory neurotransmission is necessary for critical period opening and that this involves sensory-driven maturation of excitatory drive onto fast-spiking, parvalbumin (PV^+) inhibitory interneurons (Chittajallu and Isaac, 2010; Kuhlman et al., 2013). The duration of the critical period depends on modulation of PV^+ interneuron function by different "molecular brakes" (Takesian and Hensch, 2013; Trachtenberg, 2015), and it is thought that stabilization of excitatory drive onto PV^+ cells by molecular brakes is the main factor in critical period closure (Trachtenberg, 2015). Recent research has demonstrated that the extracellular matrix (ECM) protein Narp, as well as PV^+-expressed NogoR and neuregulin 1/ErbB4 signaling, control local, intracortical excitatory inputs onto PV^+ interneurons during ODP (Gu et al., 2013; Stephany et al., 2016; Sun et al., 2016). Yet long-range, feedforward inputs from the visual thalamus activate cortical PV^+ interneurons even more strongly than pyramidal neurons (Ji et al., 2016; Kloc and Maffei, 2014) and may be crucial in critical period closure (Trachtenberg, 2015). Cell-autonomous synaptic factors that organize these thalamocortical (TC) inputs remain unknown.

Here, we identify SynCAM 1 as a cell-autonomous synaptic organizer of feedforward TC inputs onto PV^+ interneurons in V1. SynCAM 1 is a synaptogenic immunoglobulin that functions in the hippocampus to assemble and maintain synapses on both principal cells and PV^+ interneurons (Biederer et al., 2002; Park et al., 2016; Robbins et al., 2010). Mice lacking SynCAM 1 or with reduced SynCAM 1 expression in V1 PV^+ interneurons exhibit immature visual function and an ODP that extends beyond the critical period into adulthood. Remarkably, even brief knockdown of SynCAM 1 in PV^+ interneurons restores juvenile-like plasticity in adult V1. Together, our results reveal a SynCAM 1-dependent, PV^+ cell-autonomous, and synapse type-specific mechanism that actively restricts cortical plasticity in the developing and adult brain and demonstrate a central role of feedforward inputs to PV^+ interneurons in critical period closure.

RESULTS

Sensory Input Selectively Regulates Expression of the Synapse Organizer SynCAM 1 in the Visual Cortex

SynCAMs 1–4 form transsynaptic complexes throughout the brain (Fogel et al., 2007). However, only SynCAM 1 transcripts exhibit an increase in cortical expression after P15, when extensive synaptic remodeling begins in this brain region (De Felipe et al., 1997; Thomas et al., 2008). We performed quantitative immunoblotting of total homogenates and quantitative immunohistochemistry of C57BL/6 wild-type mice V1 at four main stages of development: postnatal day 7 (P7), start of synaptogenesis; P14, eye opening and peak of thalamocortical remodeling; P28,

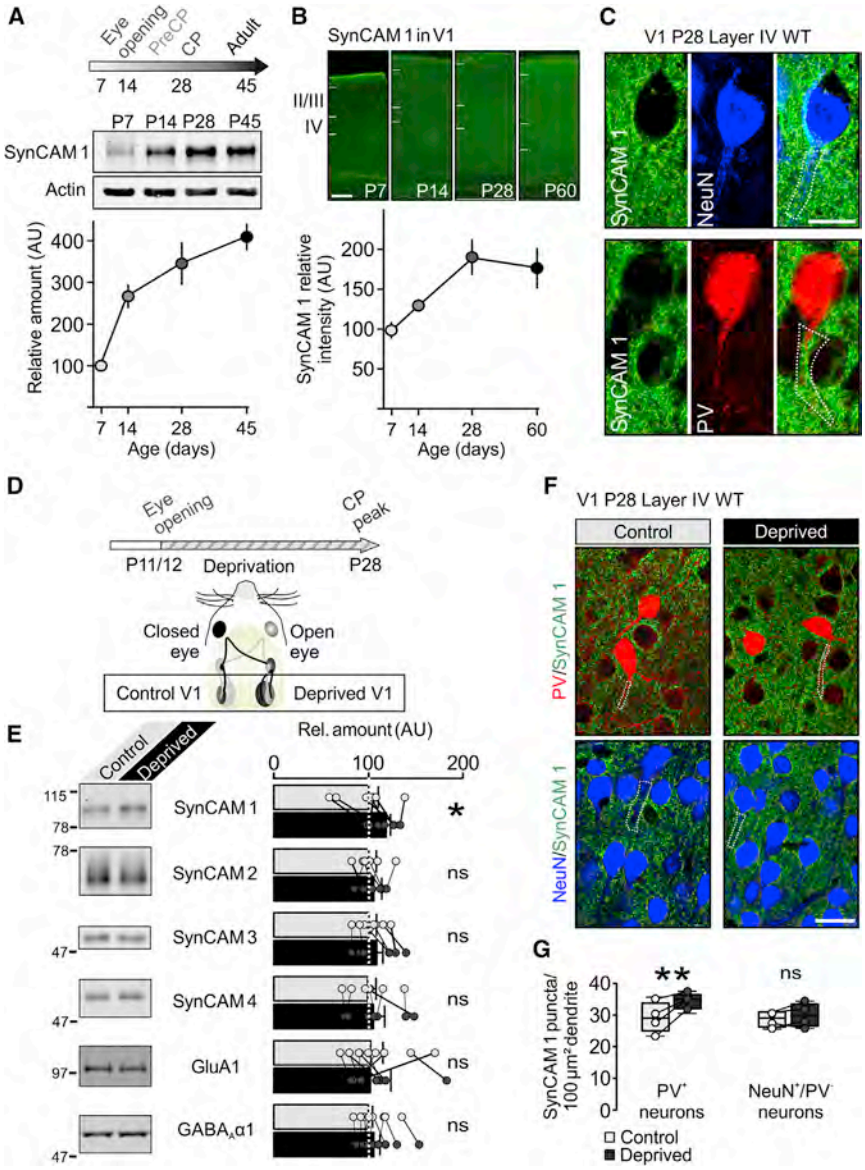

Figure 1. Expression of SynCAM 1 in V1 Is Regulated by Activity in a Cell-Specific Manner

(A) Top: time points of V1 development. Middle and bottom: quantitative immunoblotting of SynCAM 1 in the developing mouse V1 (30 µg/lane). n = 2 animals/time point. Expression levels were first normalized to actin and then to P7 levels.

(B) Top: representative maximum intensity projections of immunohistochemical staining of SynCAM 1 in the developing mouse V1. Scale bar, 250 µm. Bottom: quantification of staining intensity.

(C) SynCAM 1 antibodies stain neuropil and dendritic segments of NeuN$^+$ pyramidal neurons (top) and PV$^+$ interneurons (bottom). Single optical sections are shown. Scale bar, 15 µm.

(D) Decussation of retinal axons at the chiasm results in reduced visual responsiveness in the left visual cortex (contralateral to the deprived eye) after monocular deprivation (MD). The right visual cortex (ipsilateral) continues to receive input from the open eye and served as control in (E)–(G).

(E) Quantitative immunoblots of control and deprived P28 V1 homogenates (30 µg/lane). Molecular weights are indicated on the left. MD significantly increased SynCAM 1 in V1 but had no effect on SynCAMs 2–4 or on GluA1 and GABA$_A\alpha$R1. Measurements were first normalized to actin and then to control (ipsilateral) levels. n = 7–10 mice/experiment; ns, not significant; *p < 0.05, paired t test.

(F and G) Representative images (F) and quantification (G) of SynCAM 1 puncta on NeuN$^+$/PV$^-$ and PV$^+$ primary dendritic segments revealed a significant increase of SynCAM 1 expression in the PV$^+$ neurons of the deprived hemisphere.

n = 4 mice/experiment; **p < 0.01, two-way RM ANOVA. Scale bar, 20 µm. Data are presented as mean ± SEM (A–E) and minimum-maximum (G).

peak of the cortical critical period; and P45, young adult (Figure 1A) (Kuhlman et al., 2013). SynCAM 1 protein was detected in V1 as early as P7 (Figures 1A and 1B), after which its expression in the cortex increased strongly through P14 and P28 and remained high in adult mice (Figures 1A and 1B). To obtain insight into cell-type-specific changes, we performed immunostaining for SynCAM 1 and the neuronal nuclei marker NeuN that labels proximal dendritic segments of pyramidal neurons (Wolf et al., 1996), and parvalbumin (PV) that is detectable in dendrites of fast-spiking PV$^+$ interneurons (Kameda et al., 2012). Imaging of single optical sections showed dense SynCAM 1 puncta both on NeuN and PV-labeled dendrites (Figure 1C). This was in agreement with the reported expression of SynCAM 1 in both pyramidal neurons and PV$^+$ interneurons (Földy et al., 2016).

V1 of mice is strongly driven by contralateral eye inputs, and a blockade of visual input through one eye during the critical period for vision induces robust plasticity and remodeling in the contralateral V1 (Antonini et al., 1999; Gordon and Stryker, 1996; Heynen et al., 2003). A previous study that sought to identify candidate regulators of plasticity reported that monocular deprivation (MD) strongly upregulated SynCAM gene expression in the V1 (Lyckman et al., 2008). To determine which of the SynCAMs is regulated by MD and visual plasticity on the protein level, we performed quantitative immunoblotting of V1 in mice that had undergone MD from the beginning of eye opening until the peak of the critical period (Figure 1D) (Lyckman et al., 2008). Contralateral dominance of mouse V1 allows intra-animal comparison of changes in protein expression, where the ipsilateral cortex serves as control (Figure 1D) (Heynen et al., 2003). Only SynCAM 1 exhibited a significant activity-dependent change in protein expression (Figure 1E). MD upregulated SynCAM 1 protein levels (Figure 1E; control V1 = 100 ± 10.6 AU, deprived V1 = 121 ± 5.1 AU; p = 0.024, paired t test; n = 7 animals, t = 3, df = 6) but had no effect on SynCAM 2, 3, and 4 (Figure 1E; SynCAM 2: control = 100 ± 7.6, deprived = 106 ± 7.2; SynCAM 3: control = 100 ± 5.5, deprived = 108 ± 8.9;

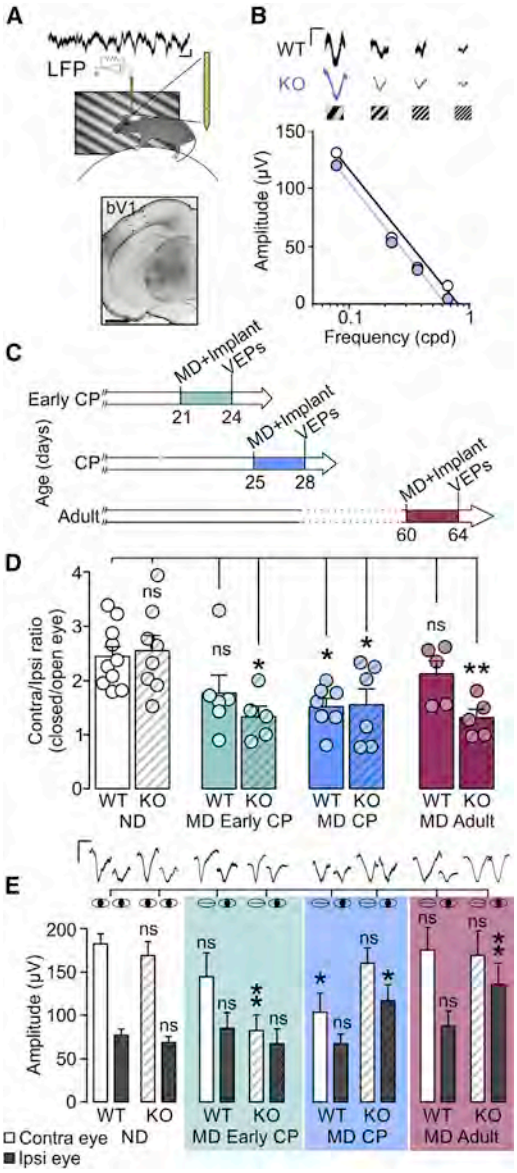

Figure 2. SynCAM 1 Limits Plasticity in the Visual Cortex

(A) Local field potentials (LFPs) evoked by full-field sinusoidal gratings or light flashes were collected using 16-channel probes (inset) from animals head-fixed over an air-suspended Styrofoam ball. Right: representative electrode tract (DiI, pink) in the binocular V1 (bV1; DAPI, grayscale).

(B) Amplitude of visually evoked responses (VEPs; top) decreases with increasing frequency of sinusoidal gratings in both wild-type (WT) and KO animals. Visual acuity was estimated for each animal by estimating the grating frequency at which the amplitude was equal to zero (WT = 0.52 ± 0.13 cpd, KO = 0.55 ± 0.03 cpd; n = 6 WT and 7 KO animals; t = 0.25, df = 11, t test; p = ns).

(C) Experimental timelines for headpost implantation for *in vivo* physiology and MD. VEPs were collected after reopening of the sutured eye. Non-deprived (ND) animals were prepared in parallel.

(D) ND SynCAM 1-KO and WT mice had indistinguishable C/I ratios. MD during the early CP resulted in a non-significant reduction of C/I in WT mice and a robust C/I reduction in KO mice. MD during the CP significantly lowered the C/I ratio in both WT and SynCAM 1-KO mice. Short MD had no effect on visual responses in adult WT mice but significantly lowered the C/I of adult SynCAM 1-KO mice.

(E) MD during the early CP caused strong depression of the closed-eye responses only in KO mice. MD during the CP significantly depressed the closed-eye responses in WT mice but increased the open eye responses in KO mice. MD in adult WT mice was without effect but significantly increased open eye responses in KO mice.

Scale bars, 250 μV and 0.5 s in (A, top), 1 mm in (A, bottom), and 100 μV and 0.2 s in (B) and (D). In (D) and (E), ns, not significant; *p < 0.05 and **p < 0.01, one-way and two-way ANOVA (see Table S1 for details). Data are presented as mean ± SEM; n values are indicated.

SynCAM 4: control = 100 ± 8.2, deprived = 107 ± 10.8; n = 7 animals; all values in AU). Consistent with previous reports (Lyckman et al., 2008; Tropea et al., 2006), deprivation did not affect the levels of glutamate or GABA receptors (Figure 1E; GluA1: control = 108 ± 13.1, deprived = 107 ± 12.5; $GABA_A\alpha1$: control = 106 ± 5.4, deprived = 112 ± 7.7; n = 10 animals; all values in AU).

To evaluate the cell-type specificity of activity-dependent changes in SynCAM 1 protein expression in the V1, we used quantitative immunohistochemistry to estimate the density of SynCAM 1 puncta in contact with $NeuN^+/PV^-$ and PV^+ dendritic segments after MD (Figures 1F, 1G, and S1). MD had a significant effect on SynCAM 1 expression (interaction between cell type and deprivation, $F_{[1,6]} = 7.53$, p = 0.03, two-way repeated-measures [RM] ANOVA), and SynCAM 1 puncta density was elevated on PV^+ dendrites in the deprived compared with the non-deprived control hemisphere (Figures 1F and 1G; control = 29 ± 2.3, deprived = 35 ± 1.3; p < 0.01, post hoc Sidak's multiple-comparisons test; n = 4 animals). We found no change in the density of SynCAM 1 puncta on $NeuN^+/PV^-$ dendrites in the deprived hemisphere (Figures 1F and 1G; control = 29 ± 1.3, deprived = 30 ± 1.8; p = ns). As a control, we performed this quantification in non-primary sensory regions on the same coronal sections used for analysis of V1 and found that the density of SynCAM 1 puncta on PV^+ dendrites in secondary auditory and ectorhinal cortex was not significantly different between the groups (Figures S1A–S1C and data not shown; control PV^+ = 31 ± 2.4, deprived PV^+ = 33 ± 1.3; control $NeuN^+/PV^-$ = 27 ± 3.1, deprived $NeuN^+/PV^-$ = 32 ± 2.7; no interaction between cell-type and deprivation on two-way RM ANOVA; $F_{[1.27,\ 3.8]} = 1.73$, p = 0.274, one-way RM ANOVA; n = 4 animals). These results supported a cell type-specific regulation of SynCAM 1 expression in V1 during ODP and suggested a role for SynCAM 1 in PV^+ interneurons during the visual critical period.

SynCAM 1 Limits Visual Plasticity in Both Juvenile and Adult Brain

Brief MD during the critical period robustly depresses closed (contralateral) eye responses in the binocular portion of mouse V1 (bV1), resulting in a strong downward shift in the contralateral/ipsilateral (C/I; closed/open) eye response ratio (Frenkel and Bear, 2004; Gordon and Stryker, 1996). PV^+ interneurons play a central role in this process (Kuhlman et al., 2013). As imbalanced visual input substantially upregulated SynCAM 1 expression on PV^+ interneurons (Figures 1F and 1G), we hypothesized that SynCAM 1 loss may modulate ODP in V1. To test this, we recorded visually evoked potentials (VEPs) from the bV1 in awake wild-type (WT) and SynCAM 1 knockout (KO) mice using 16-channel probes and a spherical treadmill setup (Figure 2A)

(Niell and Stryker, 2010). When presented with sinusoidal gratings that varied in frequency, both WT and KO animals showed the typical decrease in amplitude of VEPs evoked through the contralateral eye as the frequency of gratings increased (Figure 2B). Visual acuity was in the expected range for mice (WT = 0.52 ± 0.13 cycles per degree [cpd], KO = 0.55 ± 0.03 cpd; n = 6 WT and 7 KO animals) (Porciatti et al., 1999). We then sutured the right eyelids of KO animals and their WT littermates for 3–4 days during the early critical period (CP; P21–P24), at the peak of the critical period (P25–P28), and in adulthood (P60–P64) (Figure 2C). Non-deprived (ND) WT and KO animals had almost identical C/I ratios (Figure 2D; Table S1) and VEP amplitudes, as expected from normal acuity in KO mice (Figures 2B and 2E; Table S1). For mice that underwent MD, we reopened the sutured eyelid on the last day of deprivation and recorded visual responses to the stimulation of both closed (contralateral) and open (ipsilateral) eyes. Consistent with previous studies, 3 days of MD during the early critical period were not sufficient to significantly affect visual responses in WT animals, but they induced a robust shift in C/I ratio and strong depression of closed-eye responses during the peak of the critical period (Figures 2D and 2E; Table S1) (Frenkel and Bear, 2004; Gordon and Stryker, 1996). Short-term deprivation had no effect in adult WT animals, in agreement with reduced plasticity of the mature cortex (Kuhlman et al., 2013).

Distinct from WT mice, short MD decreased the C/I ratio at all ages tested in KO mice (Figure 2D; Table S1). Three days of deprivation in mice lacking SynCAM 1 strongly depressed closed-eye responses already during the early critical period and induced open-eye potentiation during its peak (Figure 2E; Table S1). In striking contrast to WT mice, adult KO mice exhibited robust plasticity after MD, with strong open-eye potentiation. Two-way ANOVA showed a significant interaction between genotype and deprivation in the amplitude of open (ipsilateral) eye responses ($F_{[3,44]}$ = 3.1, p = 0.035) (Table S1). MD had no effect on adult animals heterozygous for SynCAM 1 loss, indicating that a substantial reduction of SynCAM 1 expression is necessary to permit plasticity (data not shown). Furthermore, short deprivation at P17 before the critical period opens had no apparent effect on either WT or KO mice (WT C/I = 2.2 ± 0.42, KO C/I = 2.2 ± 0.35; n = 4 WT and 6 KO animals). These data demonstrated a role of SynCAM 1 in restricting the closure of the critical period, without altering the timing of the precritical period.

Formation of Perineuronal Nets Is Impaired in the Absence of SynCAM 1

The closure of the critical period in V1 requires mature PV^+-mediated cortical inhibition (Fagiolini et al., 2004; Kuhlman et al., 2013). A measure of PV^+ interneuron maturation is the formation of proteoglycan-composed ECM structures called perineuronal nets (PNNs) around them (Figure 3A) (Dityatev et al., 2007; Ye and Miao, 2013). To track this maturation process, we studied the development of PNNs in SynCAM 1-KO V1 by quantifying the staining intensity of the PNN marker *Wisteria floribunda* agglutinin (WFA) (Ye and Miao, 2013). At the start of the critical period (early CP), WT mice already had more than 60% of their PV^+ interneurons enwrapped with PNNs (Figures 3B and 3D) (WT early CP/P21 = 67 ± 6.3, n = 5 animals; WT CP/P28 = 70 ± 4.5, n = 4; WT adult/P60–P70 = 74 ± 2, n = 4; all values in % of PV^+ interneurons). The density of PNN puncta around PV^+ interneurons that were positive for PNNs steeply increased from early critical period to adulthood in WT mice (Figure 3E) (WT early CP/P21 = 301 ± 61.7, CP/P28 = 837 ± 139.3, adult/P60–P70 = 1,271 ± 113.2; all values in particles/mm^2). The overall density of PV^+ interneurons in SynCAM 1-KO mice was indistinguishable from WT mice (Figure 3F) (early CP P21 WT = 141 ± 7, KO = 140 ± 14.1; CP/P28 WT = 163 ± 10.2, KO = 168 ± 15.5; adult/P60–P70 WT = 155 ± 4.8 cells/mm^2, KO = 155 ± 8.9; all values in cells/mm^2). In contrast to the prominent enwrapping of PV^+ cells in WT mice, the fraction of PV^+ interneurons surrounded by PNNs was significantly lower in KO mice at all ages tested (Figures 3C and 3D) (early CP/P21 = 42 ± 5.5, p = 0.008; CP/P28 = 35 ± 3.7, p = 0.0006; adult/P60–P70 = 50 ± 5, p = 0.014; $F_{[5,16]}$ = 9.9, p = 0.0002, one-way ANOVA, Holm-Sidak's multiple-comparisons test). In addition, loss of SynCAM 1 severely reduced PNN deposition in those PV^+ cells that remained positive for WFA (Figures 3C and 3E) (KO early CP/P21 = 75 ± 47.5, n = 3, p = 0.415; KO CP/P28 = 178 ± 50.4, n = 3, p = 0.003; KO adult/P60–P70 = 766 ± 195.2, n = 3, p = 0.019; all values in particles/mm^2; $F_{[5,16]}$ = 17.4, p < 0.0001, one-way ANOVA, Holm-Sidak's multiple-comparisons test). We investigated the distribution of SynCAM 1 in primary cultures of cortical neurons, and its robust signal on developing and mature PV^+ interneurons did not colocalize with WFA, which argued against SynCAM 1 being a specific component of PNNs (Figure S2). Otx2, a PNN-dependent transcription factor that directs the maturation of PV^+ interneurons (Sugiyama et al., 2008), was unaltered in SynCAM 1-KO PV^+ interneurons (Figure S3). These results demonstrated impaired development of PNNs in the absence of SynCAM 1 and provided evidence that the reduced maturation of cortical PV^+ interneurons in KO mice involves an Otx2-independent mechanism.

SynCAM 1 Is Necessary for Recruitment of Thalamocortical Terminals onto PV^+ Interneurons

Excitatory synaptic input can control the deposition of PNNs around PV^+ interneurons (Dityatev et al., 2007). SynCAM 1 contributes to the development of excitatory synapses on interneurons in the hippocampus (Park et al., 2016). We therefore studied the two main types of glutamatergic inputs on cortical PV^+ interneurons: short range/intracortical and long-range/thalamocortical (TC) inputs (Figure 4A), which use presynaptic vesicular glutamate transporter 1 (vGlut1) and 2 (vGlut2), respectively (Fremeau et al., 2001; Singh et al., 2016). WT mice exhibited intense vGlut1 signal throughout the cortex, while vGlut2 appeared as a thick band in the thalamorecipient layer IV, consistent with previous studies (data not shown) (Coleman et al., 2010). We quantified the number and size of vGlut1 and vGlut2 puncta in single optical sections of PV^+ dendrites in V1 (Figures S4 and S5). The number of vGlut2 puncta in contact with PV^+ dendrites in layer IV of WT mice did not vary from early critical period (early CP/P21) to adulthood (P60–P70) in agreement with previous reports (Figures 4B and 4D) (early CP/P21 = 18 ± 0.4, n = 5 animals; CP/P28 = 17 ± 0.5, n = 4; adult/P60–P70 = 17 ± 0.7, n = 4; all values in

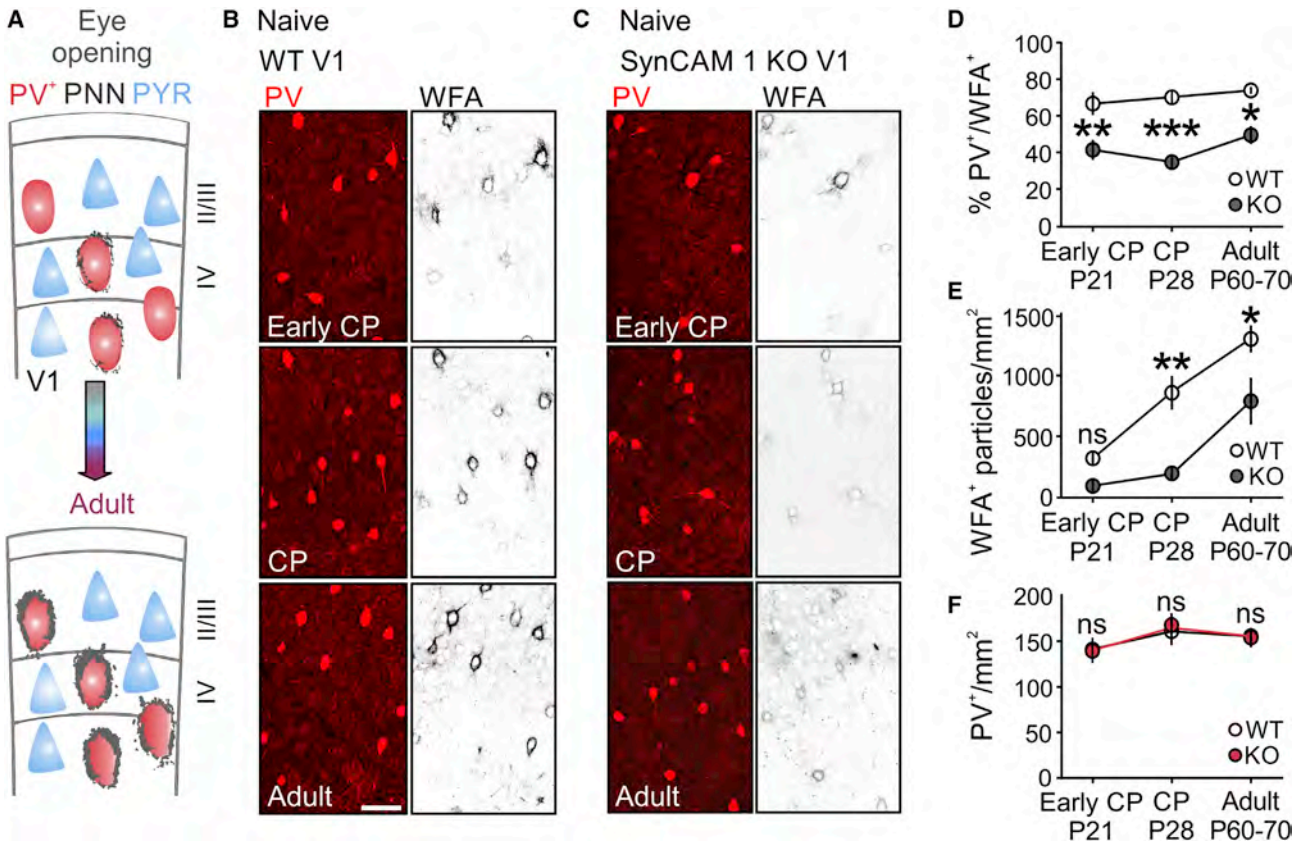

Figure 3. Formation of PNNs Is Reduced in the Absence of SynCAM 1

(A) PNN deposition increases parallel to the maturation of PV^+ interneurons after eye opening in V1. Pyramidal neurons (PYR; blue) lack PNNs.

(B) Double labeling for PV (red) and WFA (gray) in WT V1 showed that WFA^+ PNNs enwrapped the majority of PV^+ interneurons in the WT. Scale bar, 50 μm.

(C) PNNs surrounded fewer PV^+ interneurons in SynCAM 1-KO mice at all ages tested.

(D) Quantification of images as in (B) and (C) showed a significant difference in the density of WFA-positive PV^+ interneurons between genotypes through all ages tested.

(E) The density of PNNs increased throughout age in WT animals but remained significantly lower from the critical period onward in the fraction of PV^+ cells of KO mice that were positive for WFA.

(F) The density and distribution of PV^+ cells were indistinguishable between WT and SynCAM 1-KO mice.

In (D)–(F), ns, not significant; *$p < 0.05$, **$p < 0.01$, and ***$p < 0.001$, one-way ANOVA. Data are presented as mean ± SEM; n = 3–5 animals/genotype.

puncta/100 μm^2) (Kameda et al., 2012). In contrast, loss of SynCAM 1 in KO mice significantly reduced density of $vGlut2^+$ TC inputs to PV^+ dendrites from the onset of critical period onward compared with WT littermate controls (Figures 4B and 4D) (KO early CP/P21 = 16 ± 0.6, n = 3, p = 0.036, 12% reduction; CP/P28 = 14 ± 0.5, n = 3, p = 0.008, 19% reduction; adult/P60–P70 = 13 ± 1.3, n = 3, p = 0.001, 25% reduction; all values in puncta/100 μm^2; $F_{[5,16]} = 8.5$, p = 0.0004, one-way ANOVA, Holm-Sidak's multiple-comparisons test). The density of intracortical, $vGlut1^+$ inputs to PV^+ dendrites was indistinguishable between WT and KO animals at all ages (Figures 4C and 4E) (early CP/P21 WT = 35 ± 0.8, KO = 33 ± 0.9; CP/P28 WT = 31 ± 1.2, KO = 30 ± 1.8; adult/P60–P70 WT = 33 ± 1.7, KO = 34 ± 0.4; all values in puncta/100 μm^2). Puncta size was not significantly different between the groups for both vGlut1 and vGlut2 (data not shown). These results strongly supported a TC-specific input impairment in PV^+ interneurons of SynCAM 1-KO mice.

TC axons extensively arborize in cortical layer IV during early postnatal development, and their fine structure can be determined by injecting anterograde tracers into the dorsolateral geniculate nucleus of the thalamus (dLGN) (Antonini et al., 1999). To assess if arborization of TC axons was impaired, we injected an anterogradely transporting AAV-EGFP construct into dLGNs of adult WT and SynCAM 1-KO mice (Figure 4F) and reconstructed single-axonal arbors (Figure 4G). Absence of SynCAM 1 did not affect total branch length and the number of TC branches (Figures 4H and 4I). Only their variability was increased in KO mice, as measured by the coefficient of variation ($CV_{branch\ length}$: WT = 274 ± 53.98, KO = 781 ± 139.8; p = 0.015, t test; n = 4 animals, t = 3.4, df = 6; $CV_{branch\ number}$: WT = 2.2 ± 0.56, KO = 6.5 ± 0.42; p = 0.0008, t test; n = 4 animals, t = 6.2, df = 6). Together, these results supported grossly normal arborization of thalamocortical projections and select aberrations in their fine synaptic connectivity in the absence of SynCAM 1.

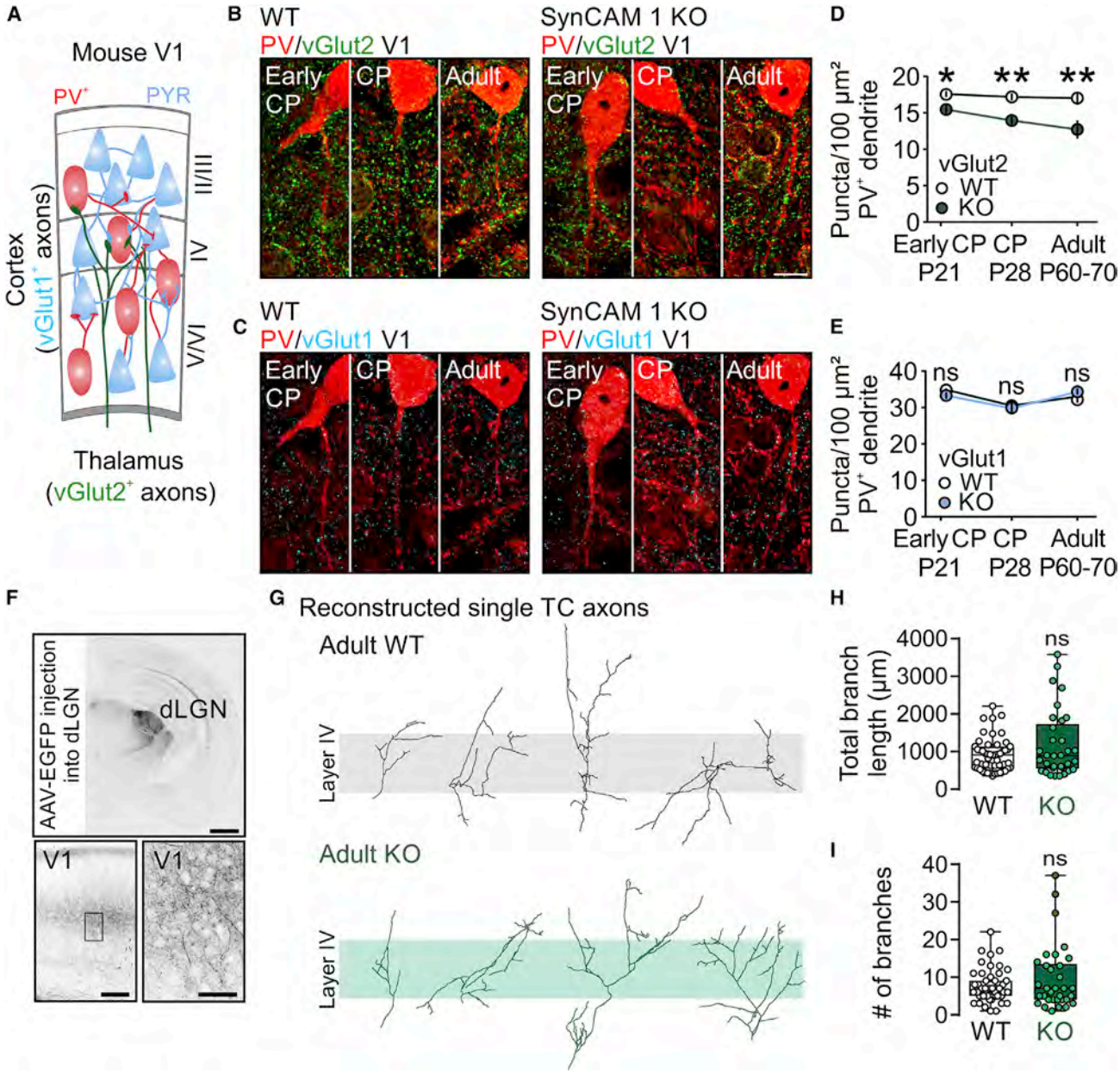

Figure 4. PV⁺ Interneurons in V1 of SynCAM 1-KO Mice Receive Fewer Inputs from Thalamus

(A) vGlut2⁺ inputs from dLGN (green) innervate both PV⁺ inhibitory neurons (red) and pyramidal neurons (blue) in layers II/III and IV. Local cortico-cortical connections predominantly use vGlut1 (cyan).

(B and C) Representative single optical sections of PV/vGlut2 (B) and PV/vGlut1 (C) immunofluorescence in layer IV V1 of WT and SynCAM 1-KO mice at the indicated ages. Scale bar, 15 μm.

(D) KO mice showed a significant reduction in TC inputs in contact with PV⁺ dendrites at all ages.

(E) Density of intracortical vGlut1⁺ inputs on KO and WT PV⁺ cells was indistinguishable.

(F) Top: anterograde AAV tracer in the dLGN. Scale bar, 500 μm. Bottom left: V1 sections from the same animal show thalamic projections in layer IV (inset). Scale bar, 250 μm. Bottom right: high magnification reveals thalamocortical arbors. Scale bar, 50 μm.

(G) Representative reconstructions of single thalamocortical axons from adult WT (top, black) and KO (bottom, green), arranged from simplest to most complex (left to right).

(H and I) Overall branch length was not significantly different between WT and KO mice (H), and neither was the branching complexity (I).

In (D) and (E), ns, not significant; *$p < 0.05$, **$p < 0.01$, and ***$p < 0.001$, one-way ANOVA. Data are presented as mean ± SEM (D and E) and minimum-maximum of all data points (H and I; indicated); n = 3–5 animals/genotype, unless indicated otherwise. In (H) and (I), ns, not significant.

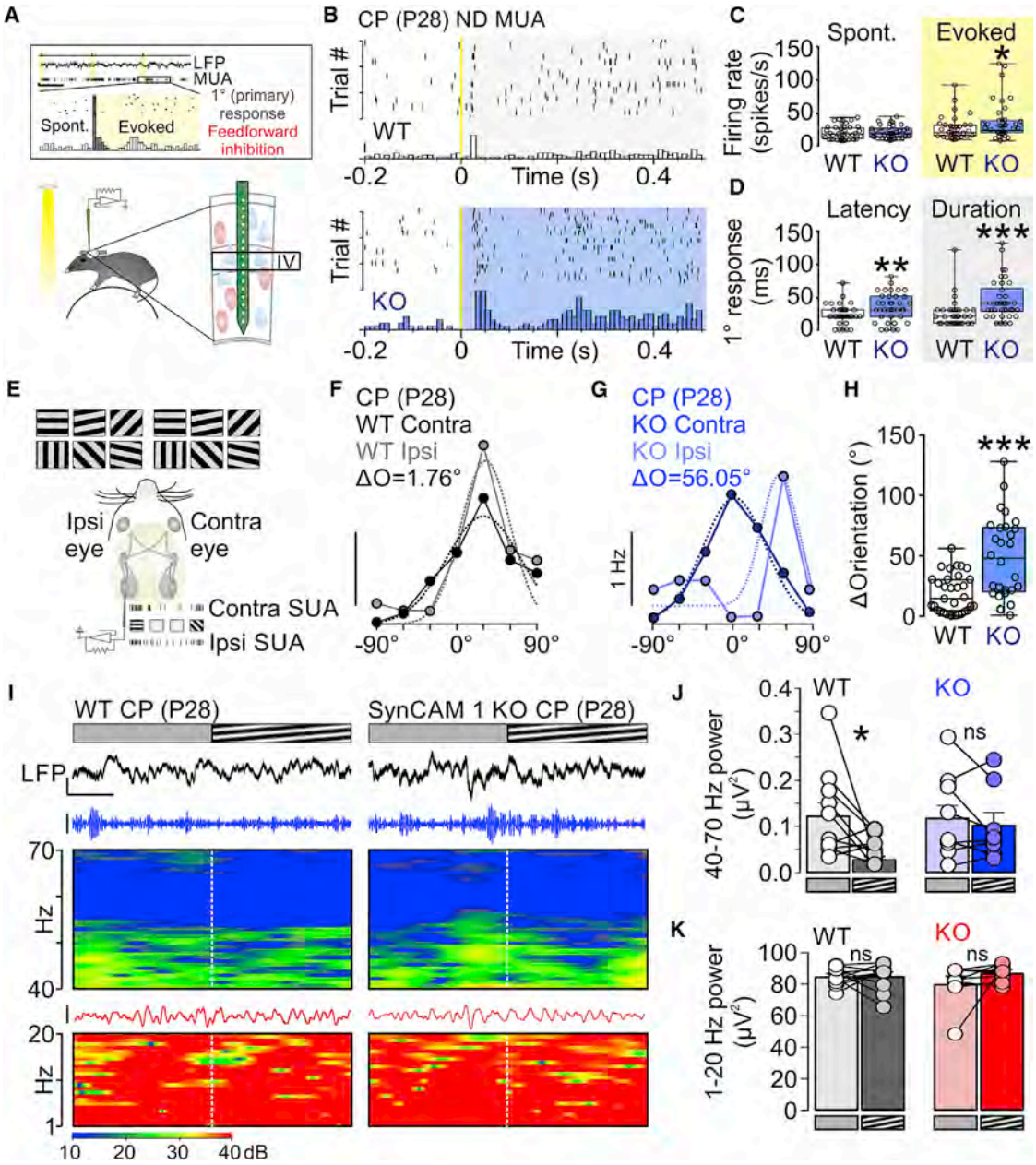

Figure 5. Feedforward Inhibition and Visual Circuit Function Are Immature in SynCAM 1-KO Mice

(A) Inset: example of spiking activity and peristimulus time histogram (PSTH) that marks measured parameters. Evoked firing rate was calculated as average spontaneous firing rate subtracted from average peak firing rate. Stimulus (LED flash) is indicated in yellow. Scale bars, 100 μV and 2.5 s.

(B) Representative raster plots and PSTHs of MUA recorded from WT (top) and SynCAM 1-KO mice (bottom) at P28, the peak of CP. Scale bar, 15 spikes/s.

(C) Average spontaneous, prestimulus firing rate was comparable in SynCAM 1-KO mice with that of WT mice (left), but the evoked firing rate was significantly increased in SynCAM 1-KO animals (right) (Table S2).

(D) Increased latency of the primary response (left) and response duration (right) in SynCAM 1-KO mice (Table S2) (n_{MUA} = 39 WT and 38 KO for C and D).

(E) Mice were presented with gratings of varying orientations through both eyes, and responses of isolated binocular neurons (single unit activity [SUA]) in V1 were isolated and compared.

(F) WT mice show overlapping binocular responses (ΔO), indicating mature binocular visual function. Dotted line represents Gaussian fit of normalized stimulus-evoked spike rate (individual points). Preferred orientation was calculated as the maximum response amplitude after the Gaussian fit. Scale bar, 1 Hz.

(G) KO mice have little overlap between contralateral and ipsilateral responses (Gaussian fit in dotted line).

(H) Binocular matching or orientation preference, determined as the difference between preferred orientations of contra and ipsi eye responses, is significantly different between WT and KO mice (n_{SUA} = 33 WT and 28 KO).

(legend continued on next page)

Maturation of the Visual Circuit Requires SynCAM 1

The reduced TC inputs onto PV$^+$ interneurons in absence of SynCAM 1 may affect the maturation of visual responses. We therefore analyzed spontaneous and stimulus-induced activity of neurons (multi-unit activity [MUA]) from layer IV VEPs (Figure 5A). Feedforward inhibition in the V1 matures after eye opening and strongly suppresses the primary response of pyramidal neurons to visual stimulation (Gu et al., 2013; Shen and Colonnese, 2016). During the critical period, both WT and KO animals showed robust and transient increases in firing rate in response to light presentation (Figure 5B). Spontaneous firing rate was indistinguishable between KO and WT mice (Figures 5B and 5C, left; Table S2). However, the stimulus-evoked firing rate was significantly increased in KO animals (Figure 5C, right; Table S2), indicating disinhibition of visual responses (Gu et al., 2013). Detailed analysis of firing revealed a primary visual response that was significantly delayed (Figure 5D, left) and protracted (Figure 5D, right) in KO animals (Table S2), where the delay in firing onset likely reflected a delayed onset of retinal responses to light in KO mice (Ribic et al., 2014; Shen and Colonnese, 2016). These results supported that feedforward inhibition in V1 is impaired in absence of SynCAM 1, consistent with the lower density of TC inputs onto PV$^+$ interneurons.

Visual function matures during the critical period such that binocularly responsive neurons in adult V1 that are selective for stimulus orientation have similar eye-specific orientation preference (Wang et al., 2010). Binocular orientation preference is poorly matched at the onset of the critical period in mouse V1 and improves in an activity-dependent manner until the critical period closes (Wang et al., 2010, 2013). As visual responses are immature in SynCAM 1-KO mice (Figures 5C and 5D), we predicted that the binocular matching of orientation preference might also be impaired in the absence of SynCAM 1. We isolated responses of single cortical neurons to sinusoidal gratings that varied in orientation (Figure 5E), and constructed orientation tuning curves for responses to the stimulation of contralateral and ipsilateral eyes (Figures 5F and 5G). Most sampled cells were selective for orientation in both WT and KO, with the orientation selectivity index (OSI) matching previous reports for critical period mice (OSI WT contralateral = 0.52 ± 0.04, WT ipsilateral = 0.38 ± 0.06; KO contralateral = 0.51 ± 0.05, KO ipsilateral = 0.46 ± 0.05; n = 33 WT and 28 KO) (Wang et al., 2013). Most cells in the WT mice also showed matched preferred orientations between contralateral and ipsilateral responses (ΔO = 18.15 ± 2.77°) (Figures 5F and 5H) (Wang et al., 2010, 2013). In contrast, cells in KO mice displayed large differences between eyes in preferred orientations (ΔO = 48.24 ± 6.45°; p = 0.0002, Mann-Whitney t test) (Figures 5G and 5H). Binocular matching of orientation preference was therefore significantly reduced in KO mice, further supporting delayed maturation of V1 in these mice.

Visual stimulation suppresses PV$^+$-mediated gamma power oscillations (>40 Hz) (Cardin et al., 2009) during the critical period in V1, which can be prevented by delaying circuit maturation with dark rearing (Chen et al., 2015). As visual circuits appeared immature in the absence of SynCAM 1 (Figures 5B–5G), we hypothesized that gamma range power might be aberrant in SynCAM 1-KO mice during the critical period. Consistent with previous studies (Chen et al., 2015), critical-period WT mice exhibited a drop in gamma power (40–70 Hz) after switching their stimulus from blank gray screen to full-field sinusoidal gratings (Figures 5I and 5J) (WT blank = 0.25 ± 0.06 μV^2, gratings = 0.09 ± 0.02 μV^2, p = 0.026; n = 11 animals; t = 2.6, df = 10, paired t test). Gamma suppression was most pronounced in layer IV ($\Delta power^{blank\text{-}gratings}$ at 400 μm, 0.21 ± 0.08 μV^2; layer II/III at 100–350 μm, 0.12 ± 0.06 μV^2; layers V/VI at 450–700 μm, 0.13 ± 0.08 μV^2). No change in the low*frequency range (1–20 Hz) was measured in WT mice after visual stimulation, as expected (Figures 5I and 5K) (WT blank, 85 ± 1.6 μV^2; gratings, 85 ± 2.6 μV^2) (Chen et al., 2015). Similar to WT mice, KO mice showed no stimulation-induced changes in the 1–20 Hz band (Figures 5I and 5K) (KO blank, 80 ± 4.7 μV^2; gratings, 87 ± 1.9 μV^2; n = 8). Notably, KO mice lacked the visual stimulation-induced suppression of gamma band activity (Figures 5I and 5J) (KO blank, 0.25 ± 0.07 μV^2; gratings, 0.21 ± 0.06 μV^2). These results provided further evidence that thalamocortical circuitry remains immature in the absence of SynCAM 1.

SynCAM 1 Acts in PV$^+$ Interneurons in V1 to Control the Maturation of the Thalamocortical Visual Circuit

Where does SynCAM 1 function to promote visual circuit maturation? We addressed this question through region- and cell type-specific manipulations. Recent studies implicated the visual thalamus in the regulation of critical period plasticity (Jaepel et al., 2017; Sommeijer et al., 2017). SynCAM 1 expression in the lateral geniculate nucleus (LGN) was low during postnatal development (Figure S6A), and the organization of LGN in SynCAM 1-KO mice was grossly normal (Figures S6B and S6C), suggesting a cortical locus of SynCAM 1 function during ODP. Cortical PV$^+$ interneurons were immature in the absence of SynCAM 1 (Figure 3) and density and PNN coverage of regular spiking interneurons detected with WFA and antibodies against somatostatin interneurons appeared normal (data not shown). To directly test whether the locus of SynCAM 1 action during ODP are PV$^+$ interneurons, we cloned an shRNA against SynCAM 1 and a control scrambled sequence into an adenoviral vector (AAV) that allows Cre-induced short hairpin RNA (shRNA) expression (Figure S7). We injected AAV at P14 to deliver shSynCAM 1 (chronic knockdown [cKD] [PV-Cre$^{AAV\text{-}shSynCAM\ 1}$]) or shScramble (control [Ctrl] [PV-Cre$^{AAV\text{-}shScramble}$]) into the left cortex of PV-Cre mice

(I) Animals were first presented with a gray screen (marked by a gray bar) and then shown sinusoidal gratings (striped bar). LFPs were filtered to depict oscillations and sonograms. Scale bars, 350 μV for LFP, 50 μV for 40–70 Hz, and 250 μV for 1–20 Hz and 0.5 s.

(J) Visual stimulation suppressed oscillations in the γ range (40–70 Hz) in WT animals during the CP, compared with gray screen presentation. This effect was absent in CP SynCAM 1-KO animals.

(K) No change in lower frequency bands (1–20 Hz) was detected in either WT or SynCAM 1-KO animals after stimulus presentation.

In (C)–(H), data are presented as minimum-maximum.*p < 0.05, **p < 0.01, and ***p < 0.001, Mann-Whitney rank-sum test. In (J) and (K), ns, not significant; *p < 0.05, paired t test. Data are presented as mean ± SEM; ns, not significant; *p < 0.05; n = 11 WT and 9 KO, paired t test.

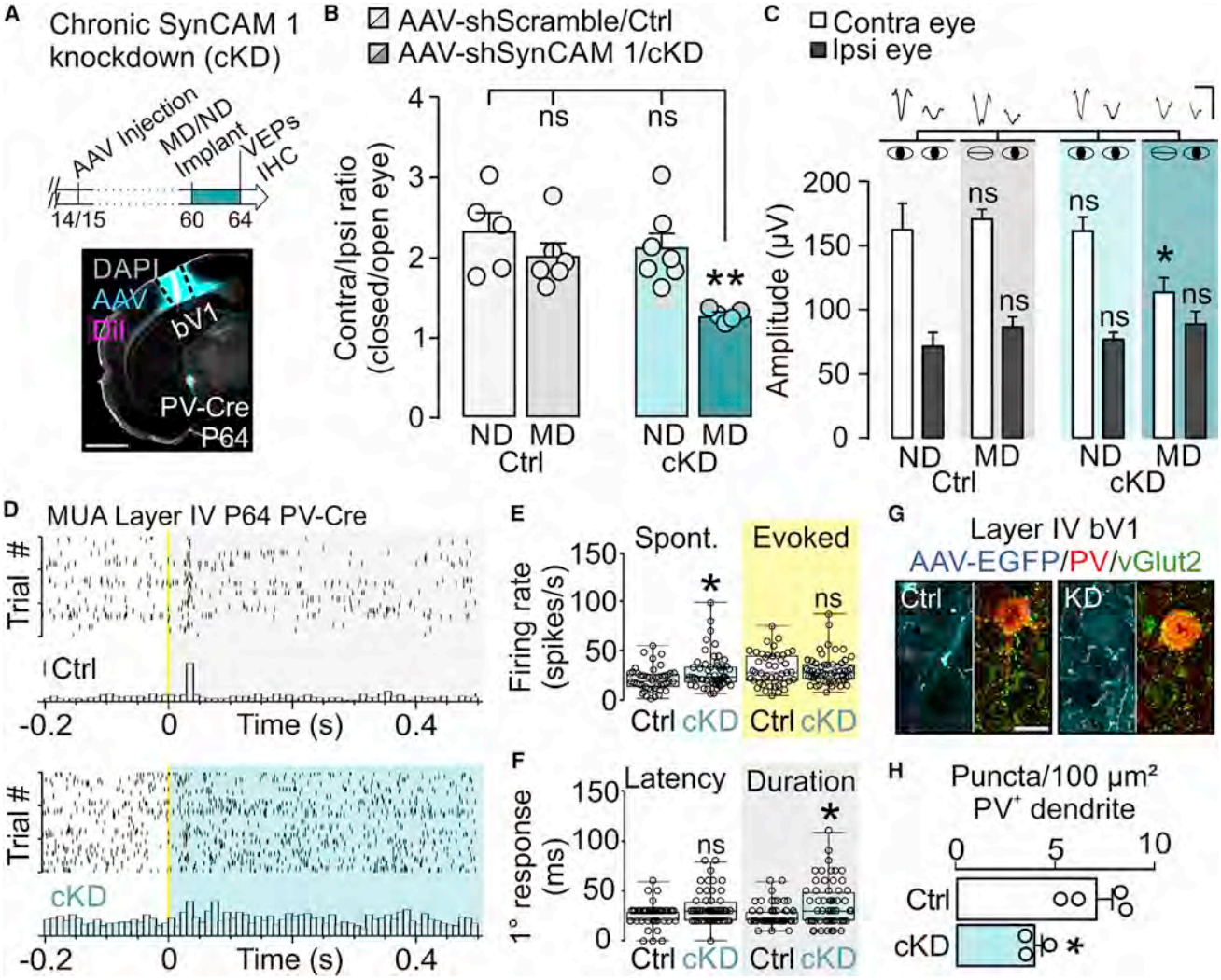

Figure 6. PV⁺ Interneuron-Specific Knockdown of SynCAM 1 in V1 Extends the Critical Period

(A) Top: experimental timeline. ND, non-implanted animals were used for immunohistochemistry (IHC). Bottom: false-colored representative section of an AAV-injected animal with visible electrode tract (AAV transduction detected by GFP shown in turquoise, DiI in magenta, and DAPI in grayscale). Scale bar, 1 mm.

(B) Chronic SynCAM 1 knockdown in PV⁺ interneurons (cKD) had no effect on C/I ratios. Four days of MD at P60 did not affect shScramble-injected control (Ctrl) animals, but MD robustly decreased the C/I ratio in cKD mice.

(C) Visual responses of naive, ND Ctrl, and cKD animals were almost identical. MD had no effect on Ctrl animals but significantly depressed closed-eye responses in cKD mice. Representative VEPs are shown on top. Scale bars, 200 μV and 0.2 s. In (C) and (D), ns, not significant; *$p < 0.05$ and **$p < 0.01$, one-way ANOVA. Data are presented as mean ± SEM; n = 5–7 animals/group.

(D) Representative raster plots and PSTHs of MUA recorded from layer IV of P64 Ctrl (top, gray) or cKD mice (bottom, green) showed that spontaneous firing rate was significantly increased in cKD mice (E, right), while the stimulus-evoked rate was not significantly different between groups (E, left). Stimulus onset is indicated in yellow in (D). Scale bar, 5 spikes/s.

(F) Latency of primary response was not different after SynCAM 1 cKD (left), but the duration was significantly increased (right). In (E) and (F), ns, not significant; *$p < 0.05$, **$p < 0.01$, and ***$p < 0.001$; Mann-Whitney rank-sum test. Data are presented as minimum-maximum of all data points.

(G) Single optical confocal sections containing dendritic segments near the injection site were analyzed by immunostaining for PV (red) and vGlut2 (green).

(H) Quantification of data as in (G) shows that cKD of SynCAM 1 significantly reduced the density of vGlut2⁺ TC terminals onto PV⁺ dendrites in V1. *$p < 0.05$, unpaired t test. Data are presented as mean ± SEM; n = 3 or 4 animals/group. Scale bar, 15 μm.

(Figure 6A), where Cre recombinase is driven by the PV promoter. We deprived the right (contralateral) eyes of adult (P60), AAV-injected PV-Cre mice and recorded VEPs and MUA after reopening the right eye 4 days later, as well as in ND animals (Figure 6A). No detrimental effects of the viral injection on C/I ratios were observed, and shScramble Ctrl and cKD animals had C/I ratio and VEP amplitudes almost identical to those of ND and non-injected WT animals during the critical period (Figures 6B and 6C; Table S3) (Ctrl ND C/I = 2.3 ± 0.2; cKD ND C/I = 2.1 ± 0.2). No gross changes in visual responses or acuity of ND mice were observed upon KD of SynCAM 1 in PV⁺ interneurons (Figures 6B and 6C; Table S3) (acuity

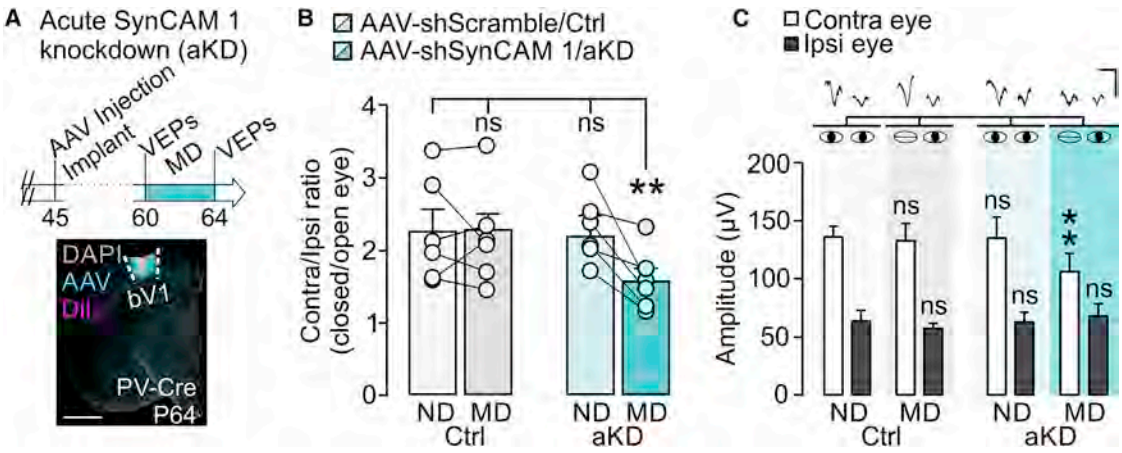

Figure 7. PV$^+$-Autonomous SynCAM 1 Actively Ctrls Plasticity in Adult Cortex

(A) Top: experimental timeline. Bottom: false-colored representative section of an AAV-injected animal with visible electrode tracts through the injection site. For section labeling, see Figure 6A. Scale bar, 1 mm.

(B) Four days of MD at P60 did not affect shScramble-injected Ctrl animals, but MD robustly decreased the C/I ratio in aKD mice.

(C) Visual responses of animals injected with shScramble Ctrl and aKD mice before MD were almost identical. MD had no effect on Ctrl animals as expected but significantly depressed closed-eye responses after aKD. Representative VEPs collected from Ctrl and aKD mice are shown on top. Scale bars, 200 μV and 0.2 s. In (B) and (C), ns, not significant; **p < 0.01, one-way or two-way RM ANOVA. Data are presented as mean ± SEM. n values are indicated in (B).

Ctrl = 0.61 ± 0.15 cpd, cKD = 0.51 ± 0.05 cpd). Short MD from P60 to P64 had no effect on the C/I ratio of adult shScramble Ctrl mice, as expected (Figures 6B and 6C; Table S3) (Ctrl MD C/I = 2 ± 0.2). In striking contrast, KD of SynCAM 1 in PV$^+$ interneurons resulted in robust plasticity in adult mice after short, 4-day MD (Figure 6B; Table S3) (cKD MD C/I = 1.3 ± 0.03). This plasticity was due to a significant depression of closed-eye responses, similar to the plasticity of WT mice during the critical period (Figure 6C, compare with Figure 2E; Table S3).

We observed an increase in MUA firing rate in layer IV in shScramble Ctrl mice at P64 compared with WT mice at P28 (Figure 6D, top, and Figure 6E, compare with Figures 5B and 5C; Table S4), reflecting the expected developmental increase in neuronal firing rates in adult animals compared with critical period mice (Chen et al., 2015). The spontaneous firing rate was even higher after chronic KD of SynCAM 1 in PV$^+$ interneurons (Figure 6D, bottom, and Figure 6E, left; Table S4), indicating disinhibition (Gu et al., 2013). The latency of visual responses was not significantly affected in cKD mice (Figure 6F, left; Table S4). However, cKD mice had significantly protracted primary visual responses, as observed in SynCAM 1-KO mice (Figure 6F, right, compare with Figure 5D, right; Table S4). Chronic KD of SynCAM 1 in cortical PV$^+$ interneurons starting at P14 was hence sufficient to maintain V1 in an immature state and extend plasticity beyond the critical period.

To address if disinhibition of V1 after KD of SynCAM 1 in PV$^+$ interneurons shares a common cellular mechanism with the global loss of SynCAM 1, we quantified the recruitment of TC terminals onto PV$^+$ dendrites in V1 of adult shScramble Ctrl and cKD mice near the AAV injection sites (Figures 6G and 6H). PV-specific KD of SynCAM 1 in V1 reduced the density of vGlut2$^+$ terminals in contact with PV$^+$ dendrites by 45% (Ctrl = 7 ± 0.5 puncta/100 μm^2, n = 4 animals; cKD = 4 ± 0.3 puncta/100 μm^2, n = 3 animals; p = 0.026, t = 3.1, df = 5). Intracortical inputs to PV$^+$ interneurons did not change, as the density of vGlut1 puncta in contact with PV$^+$ dendrites remained intact after SynCAM 1 KD (Ctrl = 34 ± 1.7 puncta/100 μm^2, cKD = 31 ± 7.7 puncta/100 μm^2). Puncta size was unaltered for both vGlut1 and vGlut2 across conditions (data not shown). The synaptic maturation of the thalamocortical visual circuit hence engages cell-autonomous, postsynaptic, and input-specific functions of SynCAM 1 in cortical PV$^+$ interneurons.

SynCAM 1 Actively Limits Cortical Plasticity in the Mature Brain

Chronic KD of SynCAM 1 in PV$^+$ interneurons retarded the development of cortical inhibition and arrested the cortex in a plastic state. To test if cortical plasticity is actively limited in the mature cortex by SynCAM 1 in PV$^+$ interneurons, we injected KD constructs into left visual cortices of P45 PV-Cre animals, after the critical period closure (Figure 7A) (Kuhlman et al., 2013). Two weeks later, we recorded the VEPs and sutured the right eyes of experimental animals after the recording session. Four days later, we reopened the sutured eye and collected VEPs to the stimulation from both eyes. Recording sites were positioned in the center of craniotomies made for AAV injections (Figure 7A, bottom) and craniotomies were kept small (less than 0.5 mm in diameter) to enable precise targeting of electrodes during the recording sessions. This approach allowed intra-animal comparison of VEPs before and after deprivation. Spontaneous and visually evoked activity were indistinguishable between shScramble Ctrl and acute KD (aKD) animals (Table S5). Similarly, acute SynCAM 1 KD did not affect C/I ratio or VEP amplitudes (Figures 7B and 7C; Table S6). As expected, 4-day MD at P60 had no significant effect on C/I ratios or VEP amplitudes of shScramble Ctrl animals (Figures 7B and 7C; Table S6). In contrast, 4-day MD after aKD of SynCAM 1 in PV$^+$ interneurons significantly decreased the C/I ratio, showing robust plasticity in adult aKD mice (Figure 7B; Table S6). This plasticity was due to

depression of closed-eye responses, similar to effects of acute reduction of inhibition in the adult cortex (Figure 7C; Table S6) (Harauzov et al., 2010). These results demonstrated that even brief downregulation of SynCAM 1 expression in matured PV^+ interneurons robustly increased plasticity in the adult brain.

DISCUSSION

Despite extensive research, the precise synaptic mechanisms of cortical critical period closure remain to be defined (Trachtenberg, 2015). Our study demonstrates a key role for SynCAM 1-dependent recruitment of thalamocortical synaptic inputs onto PV^+ interneurons in the closure of the critical period for vision. Our study identifies a synapse type-specific function of SynCAM 1 that contrasts with synaptic organizers of the neuroligin family, whose loss affects both intracortical and thalamocortical synapses (Singh et al., 2016). Previous studies demonstrated the requirement for a developmental increase of PV-mediated cortical inhibition to open the visual critical period (Fagiolini et al., 2004; Kuhlman et al., 2013), and our study suggests a key role for TC input-driven maturation of PV^+ interneurons in critical period closure.

Although less numerous than intracortical synapses onto PV^+ cells, TC synapses are much stronger so even a small reduction in their density can result in circuit disinhibition (Cruikshank et al., 2007; Ji et al., 2016; Kloc and Maffei, 2014). Both acute and chronic silencing of SynCAM 1 restore juvenile-like plasticity in the mature brain, supporting the permissive role of reduced inhibition in adult plasticity (Harauzov et al., 2010; Kuhlman et al., 2013). The differential baseline activity and plasticity of (contralateral) and open (ipsilateral) eye pathways in global KO and PV^+ cell-specific KD mouse models likely reflect additional roles of SynCAM 1 in excitatory neurons and at other synapse types. Excitatory synapses on pyramidal neurons are important for open-eye potentiation in young animals (Ranson et al., 2012), and potential contributions of SynCAM 1 to the plasticity of closed versus open eye pathways remain to be investigated. A recent model proposed that the maturation of inhibition during the critical period selectively decreases spontaneous cortical activity in favor of visually evoked activity, switching the network learning cues to external environment (Toyoizumi et al., 2013). The spontaneous/evoked ratio of SynCAM 1-KO mice is lower than in WT mice already during the critical period (data not shown), which in combination with a significantly lowered feedforward inhibition may shift cortical responses even further toward the open eye (Bono and Clopath, 2018; Kuhlman et al., 2013). The model proposed by Toyoizumi et al. (2013) further predicts that MD induces a shift in ocular dominance during the precritical period if thalamic afferents from one eye are mostly blocked. Although this remains to be tested, the robust shift in C/I ratio SynCAM 1-KO mice after MD during the early critical period is consistent with this prediction as these mice show a reduction of TC inputs already at that age.

Our results support that SynCAM 1 acts as a stabilizing factor for feedforward inputs onto PV^+ interneurons, actively limiting plasticity in both developing and adult brain. The elevated expression of SynCAM 1 in adult compared with young postnatal brain may restrict plasticity by maintaining strong TC inputs onto PV^+ cells. SynCAM 1 may also have dynamic roles at the synapse, evident in rapid increase of synaptic SynCAM 1 puncta size after LTD induction (Perez de Arce et al., 2015). In line with this, SynCAM 1 expression is elevated in input-deprived PV^+ interneurons after MD, which may reflect a response to maintain homeostasis and limit the extensive remodeling that occurs after deprivation within a physiological range (Espinosa and Stryker, 2012; Takesian and Hensch, 2013).

Expression of SynCAM 1 is not restricted to thalamorecipient layers in cortex, indicating that a presynaptic partner may confer the synapse type-specific roles of SynCAM 1 we report here. Although our data do not support a physical association between SynCAM 1 and ECM/PNN components, both homophilic and heterophilic interactions between SynCAM 1 and other SynCAM adhesion molecules across the synaptic cleft underlie its synapse-organizing roles (Fogel et al., 2007; Perez de Arce et al., 2015). The transsynaptic molecular partners for SynCAM 1 in the TC circuit can now be investigated in future studies.

In conclusion, these results demonstrate specific and nonredundant roles of synapse-organizing molecules in circuit development *in vivo*. Although recent research suggested thalamic contributions to V1 plasticity (Jaepel et al., 2017; Sommeijer et al., 2017), our study provides evidence that thalamocortical inputs to PV^+ interneurons are essential for critical period closure, in agreement with a central role of cortical inhibition in critical period regulation (Gu et al., 2013; Kuhlman et al., 2013; Stephany et al., 2016; Sun et al., 2016). Our work reveals that SynCAM 1 is a PV^+ cell-autonomous brake on cortical plasticity required for thalamocortical input-driven cortical maturation. This sheds light on the profound impacts of excitatory-inhibitory imbalance and regulatory feedback loops that are frequently implicated in neurodevelopmental disorders (Nelson and Valakh, 2015).

STAR★METHODS

Detailed methods are provided in the online version of this paper and include the following:

- KEY RESOURCES TABLE
- CONTACT FOR REAGENT AND RESOURCE SHARING
- EXPERIMENTAL MODEL AND SUBJECT DETAILS
- METHOD DETAILS
  - Antibodies
  - Tissue preparation for biochemistry and microscopy
  - Quantitative immunoblotting
  - Culturing and immunolabeling of primary neurons
  - Immunohistochemistry and confocal microscopy
  - Image quantification
  - Bulk anterograde labeling and quantification of eye-specific segregation
  - AAV cloning, packaging, purification and shRNA validation
  - Eyelid suture
  - *In vivo* electrophysiology
  - Visual stimuli, data collection and analysis
- QUANTIFICATION AND STATISTICAL ANALYSIS
- DATA AND SOFTWARE AVAILABILITY

SUPPLEMENTAL INFORMATION

Supplemental Information includes six tables and seven figures and can be found with this article online at https://doi.org/10.1016/j.celrep.2018.12.069.

ACKNOWLEDGMENTS

We thank the members of the Biederer and Crair laboratories for valuable feedback, B. Carbone for preparation of neuronal cultures, T. Momoi for providing the SynCAM 1-KO mouse line, M. Picciotto for providing AAV vectors, L. Reijmers for sharing the PV-Cre mouse line, A. DiNardo and A. Prochiantz for providing Otx2 antibody, and the CED support team for programming advice. This work was supported by NIH grants R01 DA018928 (to T.B.), R01EY015788 (to M.C.C.), R01EY023105 (to M.C.C.), U01NS094358 (to M.C.C.), and P30EY026878 (to M.C.C.) and the Knights Templar Eye Foundation (to A.R).

AUTHOR CONTRIBUTIONS

Conceptualization, A.R.; Methodology, A.R.; Software, A.R.; Investigation, A.R.; Writing – Original Draft, A.R.; Writing – Review & Editing, A.R. and T.B.; Funding Acquisition, A.R. and T.B.; Resources, M.C.C. and T.B.; Supervision, T.B.

DECLARATION OF INTERESTS

The authors declare no competing interests.

Received: January 16, 2018
Revised: November 5, 2018
Accepted: December 17, 2018
Published: January 8, 2019

REFERENCES

Antonini, A., Fagiolini, M., and Stryker, M.P. (1999). Anatomical correlates of functional plasticity in mouse visual cortex. J. Neurosci. *19*, 4388–4406.

Biederer, T., and Scheiffele, P. (2007). Mixed-culture assays for analyzing neuronal synapse formation. Nat. Protoc. *2*, 670–676.

Biederer, T., Sara, Y., Mozhayeva, M., Atasoy, D., Liu, X., Kavalali, E.T., and Südhof, T.C. (2002). SynCAM, a synaptic adhesion molecule that drives synapse assembly. Science *297*, 1525–1531.

Bono, J., and Clopath, C. (2018). Synaptic plasticity onto inhibitory neurons as a mechanism for ocular dominance plasticity. bioRxiv. https://doi.org/10.1101/280511.

Brainard, D.H. (1997). The Psychophysics Toolbox. Spat. Vis. *10*, 433–436.

Cardin, J.A., Carlén, M., Meletis, K., Knoblich, U., Zhang, F., Deisseroth, K., Tsai, L.H., and Moore, C.I. (2009). Driving fast-spiking cells induces gamma rhythm and controls sensory responses. Nature *459*, 663–667.

Chen, G., Rasch, M.J., Wang, R., and Zhang, X.H. (2015). Experience-dependent emergence of beta and gamma band oscillations in the primary visual cortex during the critical period. Sci. Rep. *5*, 17847.

Chittajallu, R., and Isaac, J.T. (2010). Emergence of cortical inhibition by coordinated sensory-driven plasticity at distinct synaptic loci. Nat. Neurosci. *13*, 1240–1248.

Coleman, J.E., Nahmani, M., Gavornik, J.P., Haslinger, R., Heynen, A.J., Erisir, A., and Bear, M.F. (2010). Rapid structural remodeling of thalamocortical synapses parallels experience-dependent functional plasticity in mouse primary visual cortex. J. Neurosci. *30*, 9670–9682.

Cruikshank, S.J., Lewis, T.J., and Connors, B.W. (2007). Synaptic basis for intense thalamocortical activation of feedforward inhibitory cells in neocortex. Nat. Neurosci. *10*, 462–468.

De Felipe, J., Marco, P., Fairén, A., and Jones, E.G. (1997). Inhibitory synaptogenesis in mouse somatosensory cortex. Cereb. Cortex *7*, 619–634.

Dityatev, A., Brückner, G., Dityateva, G., Grosche, J., Kleene, R., and Schachner, M. (2007). Activity-dependent formation and functions of chondroitin sulfate-rich extracellular matrix of perineuronal nets. Dev. Neurobiol. *67*, 570–588.

Dombeck, D.A., Khabbaz, A.N., Collman, F., Adelman, T.L., and Tank, D.W. (2007). Imaging large-scale neural activity with cellular resolution in awake, mobile mice. Neuron *56*, 43–57.

Espinosa, J.S., and Stryker, M.P. (2012). Development and plasticity of the primary visual cortex. Neuron *75*, 230–249.

Fagiolini, M., Fritschy, J.M., Löw, K., Möhler, H., Rudolph, U., and Hensch, T.K. (2004). Specific GABAA circuits for visual cortical plasticity. Science *303*, 1681–1683.

Faraji, F., Pang, Y., Walker, R.C., Nieves Borges, R., Yang, L., and Hunter, K.W. (2012). Cadm1 is a metastasis susceptibility gene that suppresses metastasis by modifying tumor interaction with the cell-mediated immunity. PLoS Genet. *8*, e1002926.

Fogel, A.I., Akins, M.R., Krupp, A.J., Stagi, M., Stein, V., and Biederer, T. (2007). SynCAMs organize synapses through heterophilic adhesion. J. Neurosci. *27*, 12516–12530.

Földy, C., Darmanis, S., Aoto, J., Malenka, R.C., Quake, S.R., and Südhof, T.C. (2016). Single-cell RNAseq reveals cell adhesion molecule profiles in electrophysiologically defined neurons. Proc. Natl. Acad. Sci. U S A *113*, E5222–E5231.

Fremeau, R.T., Jr., Troyer, M.D., Pahner, I., Nygaard, G.O., Tran, C.H., Reimer, R.J., Bellocchio, E.E., Fortin, D., Storm-Mathisen, J., and Edwards, R.H. (2001). The expression of vesicular glutamate transporters defines two classes of excitatory synapse. Neuron *31*, 247–260.

Frenkel, M.Y., and Bear, M.F. (2004). How monocular deprivation shifts ocular dominance in visual cortex of young mice. Neuron *44*, 917–923.

Fujita, E., Kouroku, Y., Ozeki, S., Tanabe, Y., Toyama, Y., Maekawa, M., Kojima, N., Senoo, H., Toshimori, K., and Momoi, T. (2006). Oligo-astheno-teratozoospermia in mice lacking RA175/TSLC1/SynCAM/IGSF4A, a cell adhesion molecule in the immunoglobulin superfamily. Mol. Cell. Biol. *26*, 718–726.

Gordon, J.A., and Stryker, M.P. (1996). Experience-dependent plasticity of binocular responses in the primary visual cortex of the mouse. J. Neurosci. *16*, 3274–3286.

Gu, Y., Huang, S., Chang, M.C., Worley, P., Kirkwood, A., and Quinlan, E.M. (2013). Obligatory role for the immediate early gene NARP in critical period plasticity. Neuron *79*, 335–346.

Harauzov, A., Spolidoro, M., DiCristo, G., De Pasquale, R., Cancedda, L., Pizzorusso, T., Viegi, A., Berardi, N., and Maffei, L. (2010). Reducing intracortical inhibition in the adult visual cortex promotes ocular dominance plasticity. J. Neurosci. *30*, 361–371.

Hermens, W.T., ter Brake, O., Dijkhuizen, P.A., Sonnemans, M.A., Grimm, D., Kleinschmidt, J.A., and Verhaagen, J. (1999). Purification of recombinant adeno-associated virus by iodixanol gradient ultracentrifugation allows rapid and reproducible preparation of vector stocks for gene transfer in the nervous system. Hum. Gene Ther. *10*, 1885–1891.

Heynen, A.J., Yoon, B.J., Liu, C.H., Chung, H.J., Huganir, R.L., and Bear, M.F. (2003). Molecular mechanism for loss of visual cortical responsiveness following brief monocular deprivation. Nat. Neurosci. *6*, 854–862.

Hippenmeyer, S., Vrieseling, E., Sigrist, M., Portmann, T., Laengle, C., Ladle, D.R., and Arber, S. (2005). A developmental switch in the response of DRG neurons to ETS transcription factor signaling. PLoS Biol. *3*, e159.

Jaepel, J., Hübener, M., Bonhoeffer, T., and Rose, T. (2017). Lateral geniculate neurons projecting to primary visual cortex show ocular dominance plasticity in adult mice. Nat. Neurosci. *20*, 1708–1714.

Ji, X.Y., Zingg, B., Mesik, L., Xiao, Z., Zhang, L.I., and Tao, H.W. (2016). Thalamocortical Innervation Pattern in Mouse Auditory and Visual Cortex: Laminar and Cell-Type Specificity. Cereb. Cortex *26*, 2612–2625.

Kameda, H., Hioki, H., Tanaka, Y.H., Tanaka, T., Sohn, J., Sonomura, T., Furuta, T., Fujiyama, F., and Kaneko, T. (2012). Parvalbumin-producing cortical interneurons receive inhibitory inputs on proximal portions and cortical excitatory inputs on distal dendrites. Eur. J. Neurosci. *35*, 838–854.

Kloc, M., and Maffei, A. (2014). Target-specific properties of thalamocortical synapses onto layer 4 of mouse primary visual cortex. J. Neurosci. *34*, 15455–15465.

Kuhlman, S.J., Olivas, N.D., Tring, E., Ikrar, T., Xu, X., and Trachtenberg, J.T. (2013). A disinhibitory microcircuit initiates critical-period plasticity in the visual cortex. Nature *501*, 543–546.

Li, H., Fertuzinhos, S., Mohns, E., Hnasko, T.S., Verhage, M., Edwards, R., Sestan, N., and Crair, M.C. (2013). Laminar and columnar development of barrel cortex relies on thalamocortical neurotransmission. Neuron *79*, 970–986.

Longair, M.H., Baker, D.A., and Armstrong, J.D. (2011). Simple Neurite Tracer: open source software for reconstruction, visualization and analysis of neuronal processes. Bioinformatics *27*, 2453–2454.

Lyckman, A.W., Horng, S., Leamey, C.A., Tropea, D., Watakabe, A., Van Wart, A., McCurry, C., Yamamori, T., and Sur, M. (2008). Gene expression patterns in visual cortex during the critical period: synaptic stabilization and reversal by visual deprivation. Proc. Natl. Acad. Sci. U S A *105*, 9409–9414.

McClure, C., Cole, K.L., Wulff, P., Klugmann, M., and Murray, A.J. (2011). Production and titering of recombinant adeno-associated viral vectors. J. Vis. Exp. (*57*), e3348.

Mohns, E.J., and Blumberg, M.S. (2008). Synchronous bursts of neuronal activity in the developing hippocampus: modulation by active sleep and association with emerging gamma and theta rhythms. J. Neurosci. *28*, 10134–10144.

Nelson, S.B., and Valakh, V. (2015). Excitatory/inhibitory balance and circuit homeostasis in autism spectrum disorders. Neuron *87*, 684–698.

Niell, C.M., and Stryker, M.P. (2008). Highly selective receptive fields in mouse visual cortex. J. Neurosci. *28*, 7520–7536.

Niell, C.M., and Stryker, M.P. (2010). Modulation of visual responses by behavioral state in mouse visual cortex. Neuron *65*, 472–479.

Park, K.A., Ribic, A., Laage Gaupp, F.M., Coman, D., Huang, Y., Dulla, C.G., Hyder, F., and Biederer, T. (2016). Excitatory synaptic drive and feedforward inhibition in the hippocampal CA3 circuit are regulated by SynCAM 1. J. Neurosci. *36*, 7464–7475.

Perez de Arce, K., Schrod, N., Metzbower, S.W.R., Allgeyer, E., Kong, G.K., Tang, A.H., Krupp, A.J., Stein, V., Liu, X., Bewersdorf, J., et al. (2015). Topographic mapping of the synaptic cleft into adhesive nanodomains. Neuron *88*, 1165–1172.

Porciatti, V., Pizzorusso, T., and Maffei, L. (1999). The visual physiology of the wild type mouse determined with pattern VEPs. Vision Res. *39*, 3071–3081.

Ranson, A., Cheetham, C.E., Fox, K., and Sengpiel, F. (2012). Homeostatic plasticity mechanisms are required for juvenile, but not adult, ocular dominance plasticity. Proc. Natl. Acad. Sci. U S A *109*, 1311–1316.

Ribic, A., Liu, X., Crair, M.C., and Biederer, T. (2014). Structural organization and function of mouse photoreceptor ribbon synapses involve the immunoglobulin protein synaptic cell adhesion molecule 1. J. Comp. Neurol. *522*, 900–920.

Robbins, E.M., Krupp, A.J., Perez de Arce, K., Ghosh, A.K., Fogel, A.I., Boucard, A., Südhof, T.C., Stein, V., and Biederer, T. (2010). SynCAM 1 adhesion dynamically regulates synapse number and impacts plasticity and learning. Neuron *68*, 894–906.

Shen, J., and Colonnese, M.T. (2016). Development of activity in the mouse visual cortex. J. Neurosci. *36*, 12259–12275.

Singh, S.K., Stogsdill, J.A., Pulimood, N.S., Dingsdale, H., Kim, Y.H., Pilaz, L.J., Kim, I.H., Manhaes, A.C., Rodrigues, W.S., Jr., Pamukcu, A., et al. (2016). Astrocytes Assemble Thalamocortical Synapses by Bridging NRX1α and NL1 via Hevin. Cell *164*, 183–196.

Slaker, M.L., Harkness, J.H., and Sorg, B.A. (2016). A standardized and automated method of perineuronal net analysis using *Wisteria floribunda* agglutinin staining intensity. IBRO Rep. *1*, 54–60.

Sommeijer, J.-P., Ahmadlou, M., Saiepour, M.H., Seignette, K., Min, R., Heimel, J.A., and Levelt, C.N. (2017). Thalamic inhibition regulates critical-period plasticity in visual cortex and thalamus. Nat. Neurosci. *20*, 1715–1721.

Sonawane, N.D., Szoka, F.C., Jr., and Verkman, A.S. (2003). Chloride accumulation and swelling in endosomes enhances DNA transfer by polyamine-DNA polyplexes. J. Biol. Chem. *278*, 44826–44831.

Stagi, M., Fogel, A.I., and Biederer, T. (2010). SynCAM 1 participates in axodendritic contact assembly and shapes neuronal growth cones. Proc. Natl. Acad. Sci. U S A *107*, 7568–7573.

Stephany, C.E., Ikrar, T., Nguyen, C., Xu, X., and McGee, A.W. (2016). Nogo receptor 1 confines a disinhibitory microcircuit to the critical period in visual cortex. J. Neurosci. *36*, 11006–11012.

Sugiyama, S., Di Nardo, A.A., Aizawa, S., Matsuo, I., Volovitch, M., Prochiantz, A., and Hensch, T.K. (2008). Experience-dependent transfer of Otx2 homeoprotein into the visual cortex activates postnatal plasticity. Cell *134*, 508–520.

Sun, Y., Ikrar, T., Davis, M.F., Gong, N., Zheng, X., Luo, Z.D., Lai, C., Mei, L., Holmes, T.C., Gandhi, S.P., and Xu, X. (2016). Neuregulin-1/ErbB4 signaling regulates visual cortical plasticity. Neuron *92*, 160–173.

Takesian, A.E., and Hensch, T.K. (2013). Balancing plasticity/stability across brain development. Prog. Brain Res. *207*, 3–34.

Thomas, L.A., Akins, M.R., and Biederer, T. (2008). Expression and adhesion profiles of SynCAM molecules indicate distinct neuronal functions. J. Comp. Neurol. *510*, 47–67.

Torborg, C.L., and Feller, M.B. (2004). Unbiased analysis of bulk axonal segregation patterns. J. Neurosci. Methods *135*, 17–26.

Toyoizumi, T., Miyamoto, H., Yazaki-Sugiyama, Y., Atapour, N., Hensch, T.K., and Miller, K.D. (2013). A theory of the transition to critical period plasticity: inhibition selectively suppresses spontaneous activity. Neuron *80*, 51–63.

Trachtenberg, J.T. (2015). Competition, inhibition, and critical periods of cortical plasticity. Curr. Opin. Neurobiol. *35*, 44–48.

Tropea, D., Kreiman, G., Lyckman, A., Mukherjee, S., Yu, H., Horng, S., and Sur, M. (2006). Gene expression changes and molecular pathways mediating activity-dependent plasticity in visual cortex. Nat. Neurosci. *9*, 660–668.

Ventura, A., Meissner, A., Dillon, C.P., McManus, M., Sharp, P.A., Van Parijs, L., Jaenisch, R., and Jacks, T. (2004). Cre-lox-regulated conditional RNA interference from transgenes. Proc. Natl. Acad. Sci. USA *101*, 10380–10385.

Villasana, L.E., Klann, E., and Tejada-Simon, M.V. (2006). Rapid isolation of synaptoneurosomes and postsynaptic densities from adult mouse hippocampus. J. Neurosci. Methods *158*, 30–36.

Wang, B.S., Sarnaik, R., and Cang, J. (2010). Critical period plasticity matches binocular orientation preference in the visual cortex. Neuron *65*, 246–256.

Wang, B.S., Feng, L., Liu, M., Liu, X., and Cang, J. (2013). Environmental enrichment rescues binocular matching of orientation preference in mice that have a precocious critical period. Neuron *80*, 198–209.

Wohleb, E.S., Wu, M., Gerhard, D.M., Taylor, S.R., Picciotto, M.R., Alreja, M., and Duman, R.S. (2016). GABA interneurons mediate the rapid antidepressant-like effects of scopolamine. J. Clin. Invest. *126*, 2482–2494.

Wolf, H.K., Buslei, R., Schmidt-Kastner, R., Schmidt-Kastner, P.K., Pietsch, T., Wiestler, O.D., and Blümcke, I. (1996). NeuN: a useful neuronal marker for diagnostic histopathology. J. Histochem. Cytochem. *44*, 1167–1171.

Ye, Q., and Miao, Q.L. (2013). Experience-dependent development of perineuronal nets and chondroitin sulfate proteoglycan receptors in mouse visual cortex. Matrix Biol. *32*, 352–363.

STAR★METHODS

KEY RESOURCES TABLE

REAGENT or RESOURCE	SOURCE	IDENTIFIER
Antibodies		
Mouse anti-Actin, 1:4000 (IB)	MP Biomedicals, Solon, OH	RRID: AB_2335304
Mouse anti-GABA-A-α1, 1:1000 (IB)	NeuroMab, University of California Davis, CA	RRID: AB_2187693
Mouse anti-GluA1. 1:1000 (IB)	NeuroMab, University of California Davis, CA	RRID: AB_2315840
Mouse anti-NeuN, 1:500 (IHC)	EMD Milipore Sigma, Darmstadt, Germany	RRID: AB_2298772
Mouse anti-Otx2, 1:20 (IHC)	Provided by Dr. Ariel DiNardo	clone CD4; RRID: AB_2313773
Goat anti-Parvalbumin, 1:500	Swant, Belinzona, Switzerland	RRID: AB_2650496
Mouse anti-Parvalbumin, 1:1000 (IHC)	EMD Milipore Sigma, Darmstadt, Germany	RRID: AB_477329
Chicken anti-SynCAM 1, 1:500 (ICC/IHC), 1:2000 (IB)	MBL Laboratories, Nagoya, Japan	RRID: AB_592783
Chicken anti-SynCAM 1, 1:1000 (IHC, IB)	Fogel et al., 2007	RRID: AB_2721136
Rabbit anti-SynCAM 2, 1:1000 (IB)	Fogel et al., 2007	RRID: AB_2721137
Rabbit anti-SynCAM 3, 1:1000 (IB)	Fogel et al., 2007	RRID: AB_2721138
Rabbit anti-SynCAM 4, 1:1000 (IB)	Fogel et al., 2007	RRID: AB_2721139
Mouse anti-VGlut1, 1:200 (IHC)	NeuroMab, University of California Davis, CA	RRID: AB_2187693
Guinea pig anti-VGlut2, 1:500 (IHC)	EMD Milipore Sigma, Darmstadt, Germany	RRID: AB_2665454
Anti-chicken Alexa 488, 1:1000 (IHC)	ThermoFisher	RRID: AB_2534096
Anti-chicken Alexa 647, 1:1000 (IHC)	ThermoFisher	RRID: AB_11194678
Anti-guinea pig Alexa 488, 1:1000 (IHC)	ThermoFisher	RRID: AB_10893081
Anti-guinea pig Alexa 647, 1:1000 (IHC)	ThermoFisher	RRID: AB_10894751
Anti-goat Alexa 647, 1:1000 (IHC)	ThermoFisher	RRID: AB_10892959
Anti-goat Rhodamine, 1:1000 (IHC)	ThermoFisher	RRID: AB_11148892
Anti-IgG1 Alexa 488, 1:1000 (IHC)	ThermoFisher	RRID: AB_2434013
Anti-IgG Alexa 647, 1:4000 (IB)	ThermoFisher	RRID: AB_2536165
Anti-IgG1 Alexa 568, 1:1000 (IHC, 1:4000 (IB)	ThermoFisher	RRID: AB_141611
Anti-IgG2a Alexa 568, 1:4000 (IB)	ThermoFisher	RRID: AB_2535773
Anti-chicken IRDye800, 1:4000 (IB)	Rockland	RRID: AB_1660856
Anti-rabbit IRDye800,:4000 (IB)	Rockland	RRID: AB_1660971
Chemicals, Peptides, and Recombinant Proteins		
CTB Alexa 488	Invitrogen, Carlsbad, CA	RRID: C-22841
CTB Alexa 555	Invitrogen, Carlsbad, CA	RRID: C-22843
DAPI	EMD Milipore Sigma, Darmstadt, Germany	RRID: D9542
DiI	EMD Milipore Sigma, Darmstadt, Germany	RRID: 42364
WFA-Fluorescin	Vector Laboratories, Burlingame, CA	RRID: AB_2336875
Critical Commercial Assays		
BCA protein assay	Thermo Scientific	RRID: 23225
REDExtract-N-Amp Tissue PCR Kit	EMD Milipore Sigma, Darmstadt, Germany	RRID: XNAT
KAPA Mouse Genotyping Kit	KAPA Biosystems, Wilminton, MA	RRID: KR0385

(*Continued on next page*)

Continued

REAGENT or RESOURCE	SOURCE	IDENTIFIER
Deposited Data		
Synapse-selective control of cortical maturation and plasticity by Parvalbumin-autonomous action of SynCAM 1	Mendeley Data	https://doi.org/10.17632/9wdt9rvhck.2
Experimental Models: Cell Lines		
HEK293	ATCC	RRID: CVCL_0045
AAV-293	Stratagene	RRID: CVCL_6871
Experimental Models: Organisms/Strains		
Mouse/C57BL/6	Charles River Laboratories	RRID: IMSR_JAX:000664
Mouse/RA175	Dr. Takashi Momoi	NA
Mouse/PV-Cre	The Jackson Laboratory	RRID: IMSR_JAX:008069
Oligonucleotides		
17283 AAA TGC TTC TGT CCG TTT GC	The Jackson Laboratory	PV-Cre
oIMR9377 ATG TTT AGC TGG CCC AAA TG	The Jackson Laboratory	PV-Cre
oIMR8290 CAG AGC AGG CAT GGT GAC TA	The Jackson Laboratory	PV-Cre
oIMR8291 AGT ACC AAG CAG GCA GGA GA	The Jackson Laboratory	PV-Cre
AG0002 GAG TGA TTA ACA ACG TGC AGG CAA	This study	Ra175/SynCAM 1 KO
AG0003 ACC TGC AGG CAT GCA AGC TTG TAC	This study	Ra175/SynCAM 1 KO
AG0006 GAT GTG TGC TGA CTT AGG AAC GGT C	This study	Ra175/SynCAM 1 KO
SynCAM 1 TCC TGT TCA TCA ATA ACC TAA ACT TCA AGA GAG TTT AGG TTA TTG ATG AAC AGG TTT TTT C	This study; based on Faraji et al., 2012	shSynCAM 1
Scramble TAC ACC AAT CGC AAT ATT ACT TCT TCA AGA GAG AAG TAA TAT TGC GAT TGG TGT TTT TTT C	This study	shScramble
Recombinant DNA		
pCALNL-DsRed	Addgene	13769
pSico	Addgene	11578
AAV-GFP/Cre	Addgene	49056
pAAV-CaMKII-EGFP	Addgene	50469
AAV-dsRed-Sico	Dr. Marina Picciotto	N/A
Software and Algorithms		
Mean Variance Analysis (Torborg and Feller, 2004)	Dr. Michael C. Crair	N/A
Spike2	Cambridge Electronics Design	RRID: SCR_000903
Psychtoolbox-3	Brainard, 1997	RRID: SCR_002881
ImageJ	NIH	RRID: SCR_003070
Pipsqueak (ImageJ)	Slaker et al., 2016	http://sites.imagej.net/PIPSQUEAK/

CONTACT FOR REAGENT AND RESOURCE SHARING

Further information and requests for resources and reagents should be directed to and will be fulfilled by the Lead Contact, Thomas Biederer (thomas.biederer@tufts.edu).

EXPERIMENTAL MODEL AND SUBJECT DETAILS

Animals. Experiments were performed on C57BL6/J WT mice (The Jackson Laboratory, Bar Harbor, ME), SynCAM 1 KO mice (Fujita et al., 2006) and their WT littermates, and heterozygous PV-Cre mice (JAX 008069) (Hippenmeyer et al., 2005; Kuhlman et al., 2013). SynCAM 1 KO and PV-Cre mice were maintained on a C57BL/6N background (Charles River) and KO mice had been backcrossed more than 10 times. Animals of both sexes from P7 to P70 were used for all experiments as indicated below and stated in the figure legends. Animals were randomly assigned to experimental groups. Littermates were compared in all experiments and the experimenter was blind to the genotype or group of animals used. Animals were kept on a 12/12 hour light/dark cycle with food and water *ad libitum*. All experiments were performed during the light phase (7 AM-7 PM). For neuronal cultures, pregnant Sprague-Dawley rat

dams were purchased from Charles River Laboratories (Wilmington, MA). Animals were treated in accordance with Institutional Animal Care and Use Committee guidelines.

METHOD DETAILS

Antibodies

Primary antibodies and their properties are listed in Key Resources Table. For all immunostainings, secondary antibodies were applied in the absence of primary antibodies as a control. Secondary antibodies and reagents are listed in Key Resources Table.

Tissue preparation for biochemistry and microscopy

Animals were anesthetized with ketamine (100 mg/kg) and xylazine (10 mg/kg) in saline. For protein isolation (animals aged P7-P45 for Figure 1A and P28 for Figures 1F and 1G), visual cortices were isolated according to stereotactic coordinates (0.5-1 mm anterior to λ, 2-3 mm lateral to midline) followed by sonication in 8 M urea. For LGN isolation, forebrain was flash frozen over liquid nitrogen and later dissected on an iced platform. LGN was visually identified and isolated with a tapered scalpel blade. For GABA and glutamate receptor immunoblots, crude synaptoneurosomes were prepared as described (Villasana et al., 2006). Protein concentrations were determined using the BCA method (Thermo-Fisher Scientific, Holtsville, NY). For microscopy, animals (P7-P70, as indicated in figure legends) were transcardially perfused first with ice cold PBS and then with 4% PFA (in PBS, pH 7.4). Brains were isolated and postfixed overnight in 4% PFA and washed overnight in PBS (all at 4°C). Brains were then embedded in 3% agarose in PBS and sectioned at 40-60 μm using vibrating microtome (Leica VT1000, Leica Biosystems, Nussloch, Germany or Vibratome 1500, Harvard Apparatus, Holliston, MA). Sections were stored in PBS with 0.01% sodium azide (Sigma-Aldrich, St. Louis, MO) at 4°C.

Quantitative immunoblotting

Proteins from cortical homogenates or crude synaptosomes (10-30 μg for V1 and 60 μg for LGN, prepared as described above) were subjected to immunoblotting using standard procedures (Fogel et al., 2007) and scanned with either Odyssey Infrared Imaging System (LI-COR Biosciences, Lincoln, NE) or FluorChem M (Protein Simple, San Jose, CA). Antibodies used are listed in Key Resource Table. YUC8 and 3E1 provided almost identical signal in blots, except that SynCAM 1 signal in the LGN was better visible with YUC8, likely due to its higher affinity for different glycosylation states of SynCAM 1 (Fogel et al., 2007). For all blots imaged using FluorChem M, milk was replaced with BSA (Sigma) for blocking and probing. For quantitative immunoblotting in Figure 1, secondary IRDye800 antibodies or anti-IgG Alexa 647 were used. Quantification was performed using the gel analysis plugin in ImageJ, where actin served as loading control for all samples. Quantification was always performed blind to the experimental group.

Culturing and immunolabeling of primary neurons

Cortical neurons were prepared from rats at E18 as described (Biederer and Scheiffele, 2007) with modifications. In brief, dissected cortices were incubated in 0.05% trypsin at 37°C for 20 minutes (Invitrogen, Carlsbad, CA; 25300054) and plated at a density of ~30,000 cells per coverslip. Dissociated cells were plated on poly-l-lysine (Sigma P1274) and incubated in a cell culture incubator with 5.0% CO_2. Cytosine arabinoside (Sigma C1768) was added at a final concentration of 2 μM per well 2 days *in vitro* to prevent glia cell overgrowth. Cells were washed with ice-cold PBS and fixed at DIV 7 and DIV 14 in ice-cold 4% PFA/4% sucrose for 15 minutes, permeabilized with 0.1% Triton X-100 in PBS for 10 minutes at RT and blocked in 5% FBS in PBS for 1 hour at RT. Coverslips were later sequentially incubated for 1 hour at RT in anti-SynCAM 1, anti-Parvalbumin and WFA (see Key Resource Table for more details) and their corresponding secondary antibodies. All antibodies were diluted in PBS and coverslips were washed 3x10 minutes in PBS at RT in between all antibody incubations. Coverslips were mounted with Aqua-Mount (Polysciences Inc., Warrington, PA) and imaged as described below.

Immunohistochemistry and confocal microscopy

Primary antibodies used in double- and triple-labeling experiments were applied sequentially and blocking steps were performed using normal horse serum. Visual cortex sections were first washed in PBS and non-specific antibody binding sites were blocked with 3% normal serum and 0.03% Triton X-100 (Sigma) in PBS for 1 h at RT. Primary and secondary antibodies were diluted in 3% normal serum and 0.03% Triton X-100 in PBS and incubated either for 24-48 hours at 4°C (primary antibodies) or 1 hour at room temperature (secondary antibodies). After the antibody incubation steps, sections were washed in PBS and floated on slides in distilled water before coverslipping with mounting medium (Aqua-Polymount, Polysciences Inc., Warrington, PA, USA). Confocal microscopy was performed on a Leica TCS SPE DM2500 microscope or a Leica TCS SP8. Images were acquired with HC PL Fluotar 10x0.30 for Figure 1B, ACS AP 40x oil lens with 1.15 NA for Figures 3, 4G, S2 and S3 or ACS APO 63x oil lens with 1.3 NA for Figures 1, 4, 6 and Figure S1 using identical settings for each group within an experiment. For quantitative immunohistochemistry of synaptic markers, only single optical sections were acquired. For quantification of SynCAM 1 expression during V1 development (Figure 1B), high resolution images were taken at 5 μm intervals through the entire section. For imaging of thalamocortical axons, bV1 area encompassing Layers II/III-V was imaged using 0.5 μm steps through the entire section. All images were acquired in binocular V1, layer IV. Low magnification images were acquired with Zeiss Axio Scope (Carl Zeiss, Jena, Germany) or BZ-X700 (Keyence, Osaka, Japan).

Image quantification

For all quantifications, only single optical sections were used, except for Figure 1B, where maximum intensity projection images were used. For Figure 1, integrated density of SynCAM 1 signal was measured throughout the cortex using ImageJ (NIH) and later normalized to NeuN integrated density to correct for differences in tissue thickness. For Figure S3, Otx^+, WFA^+ and PV^+ cells were counted manually using ImageJ (NIH, Bethesda, MD). Quantification of WFA^+ puncta density was performed semi-automatically using Pipsqueak plugin for ImageJ on single optical sections (Slaker et al., 2016). Quantification of vGlut1, vGlut2 and SynCAM 1 puncta was performed as previously described (Park et al., 2016) and as outlined in Figures S1, S4 and S5. Briefly, contours of primary and secondary PV^+ or primary NeuN+/PV-dendrites in layer IV were manually outlined and served as ROI. vGlut1, vGlut2 and SynCAM 1 images were thresholded, binarized and the density of puncta in contact with PV^+ dendrites (within the ROI) was counted using particle analyzer tool with a vGlut1 and SynCAM 1 cutoff of 0.1 μm^2 and vGlut2 cutoff of 0.2 μm^2, as outlined in Figures S1, S4 and S5. On average, 10-20 dendritic segments were collected from each animal from 3-6 brain sections. For SynCAM 1 KD validation *in vivo*, ROI was defined as PV^+ cell body and 20 cells on average were analyzed per animal for both SynCAM 1 KD/PV-$Cre^{AAV\text{-}shSynCAM\ 1}$ and Control/PV-$Cre^{AAV\text{-}shScramble}$.

For tracing of single thalamocortical axons, Simple Neurite Tracer plugin for ImageJ was used (Longair et al., 2011). Briefly, axons entering layer IV were followed from their starting point to their end point by scrolling through the entire Z- stack of images. Axons with no clear point of origin or end and axons ending abruptly were not included in analyses. On average, 10 axons per animal were reconstructed.

Image collection and analyses were performed blind to the genotype or experimental group, where samples were usually coded by the animal number from the animal census. All values were checked for normal distributions and averaged per animal before final statistical analysis, unless indicated otherwise.

Bulk anterograde labeling and quantification of eye-specific segregation

Retinal ganglion cell projections from the right and the left eye were bulk labeled with CTB Alexa 488 and CTB-Alexa 555. The tracer was diluted to 1 mg/ml in 0.9% saline. At P12/13, mice were anesthetized and injected with 1–2 μL tracer per eye using a glass pulled pipette and Nanoject (Drummond Scientific, Broomall, PA). 48 hours later mice were transcardially perfused and the brains were fixed overnight in 4% PFA. Coronal sections (80 μm thickness) were collected with a vibratome as described above, mounted in Aqua-mount and imaged with a CCD camera (Zeiss). Analysis of segregation of contralateral and ipsilateral projections in dLGN was performed as previously described (Torborg and Feller, 2004). Briefly, images were background subtracted with a rolling ball radius of 200 in ImageJ, and the three sections with the largest ipsilateral (Alexa 555 labeled) area were used for analysis. The logarithm of the intensity ratio, $R = \log_{10}$ (ipsilateral channel fluorescence intensity/contralateral channel fluorescence intensity), was determined for each pixel, and a segregation index for each animal was computed as the mean of the variance of the distribution of R values. A larger segregation index (higher variance) is indicative of better segregation (Torborg and Feller, 2004).

AAV cloning, packaging, purification and shRNA validation

For SynCAM 1 KD *in vivo*, sequence shSynCAM 1 (Faraji et al., 2012) was cloned into pAAV-dsRed-Sico-shRNA (Wohleb et al., 2016) (kindly provided by Dr. Marina Picciotto, Yale University). 70% confluent AAV-HEK293 cells (Agilent, Santa Clara, CA) were transfected with pHelper, AAV/DJ Rep-Cap and pAAV-dsRed-Sico-shSynCAM 1 or pAAV-dsRed-Sico-shScramble using PEI method (Sonawane et al., 2003). Cells were collected after 72 hours and AAV was purified using iodixanol gradient (Hermens et al., 1999). AAV was further concentrated using Amicon 15 (EMD Milipore Sigma). Titer was determined as in (McClure et al., 2011). 600 nL of virus ($3x10^{12}$ GC/ml) was injected at 1 nl/s into layer 4 of bV1 (~350 μm depth) at P14 or at P45 using stereotaxic apparatus (Stoelting, Wood Dale, IL) and glass pipette attached to Hamilton syringe (Hamilton Robotics, Reno NV) using micro-syringe pump (Micro4, WPI, Sarasota, FL) at following coordinates: 0-1 mm anterior to λ, 2.5-3 mm lateral to midline. For targeting validation *in vitro*, shSynCAM 1 sequence was cloned into pSico (Ventura et al., 2004). Confluent HEK293 cells were transfected with pCAGGS-SynCAM 1 (Stagi et al., 2010), pSico-SynCAM 1 and pAAV-GFP-Cre (kindly provided by Dr. Dong Kong, Tufts University) using PEI transfection. Cells were collected 72 hours later and lysed in RIPA buffer. 30 μL of protein homogenate was immunoblotted for SynCAM 1 and quantified as described above. For targeting validation in cultured neurons, primary cortical cultures were transfected at DIV 5 as above using Lipofectamine (Invitrogen) and fixed at DIV 14. SynCAM 1 signal was quantified as described above. For targeting validation *in vivo*, animals injected with pAAV-dsRed-Sico-shSynCAM 1 or pAAV-dsRed-Sico-shScramble were perfused as described above. SynCAM 1 immunohistochemistry was described as above and puncta were quantified using PV^+ soma signal as ROI (as described above) with the experimenter blind to the experimental group.

For anterograde tracing of thalamocortical projections, 500 nL of pAAV-CaMKII-EGFP (purified as described above) was injected into both left and right dLGNs (2.10 mm posterior to Bregma, 2.19 mm lateral to midline and 2.8 mm deep) of 6-8 weeks old WT and SynCAM 1 KO mice, using Hamilton Neuros syringe (tapered, 33 G; Hamilton, Reno, NV). Animals were perfused with ice cold PBS followed by 4% PFA as described above and brains were sliced using a vibrating microtome at 80 μm thickness.

Eyelid suture

Mice were anesthetized with isoflurane in oxygen (2% induction, 1.0%–1.8% maintenance) and placed under a surgical microscope. Area around the right eye was sterilized with alcohol swabs and lid margins were trimmed. Three mattress stitches were placed using

7-0 nylon sutures and the lids were further attached using VetBond (3M). After that, ophthalmic antibiotic ointment was applied to the suture. Mice were monitored daily for the integrity of the sutures and signs of infection. Animals whose eyelids were not fully sutured and animals that removed their sutures were excluded from further experiments. At the end of the deprivation period, after the head-plate implantation (see below), the stitches were removed, and lid margins separated. Eyes were flushed with sterile saline and checked for clarity. Mice with corneal opacities, cataracts or signs of infection were excluded from further study.

In vivo electrophysiology

Recordings were performed on awake female and male mice, ages P21 to P64, using spherical treadmill as described in (Niell and Stryker, 2010). 4-7 days before the recording session (15 days for Figure 7), custom made titanium or aluminum (for precritical period mice) head-plate implants were cemented to the mouse skull. Animals were anesthetized with isoflurane in oxygen (2% induction, 1.0%–1.8% maintenance), warmed with a heating pad at 38°C and given subcutaneous injections of Buprenorphine SR (1 mg/kg) and 0.25% Bupivacaine (locally). Eyes were covered with Puralube (Decra, Northwich, UK). Scalp and fascia from Bregma to behind lambda were removed, and the skull was cleaned, dried and covered with a thin layer of cyanoacrylate (VetBond; 3M, Maplewood, MN) before attaching the head plate with dental cement (RelyX, 3M). The well of the head plate was filled with silicone elastomer (Reynold Advanced Materials, Brighton, MA) to protect the skull before recordings. Animals were single housed after the implantation and monitored daily for signs of shock or infection. 1-2 days before the recording, the animals underwent 1-2 20-30 minutes handling sessions and 1-2 10-20 minutes session in which the animals were habituated to the spherical treadmill (Dombeck et al., 2007). On the day of recording, the animals were anesthetized as above and small craniotomies (~0.5 mm in diameter) with 18G needles were made above bV1 and cerebellum. The brain surface was covered in 2%–3% low melting point agarose (Promega, Madison, WI) in sterile saline and then capped with silicone elastomer. Animals were allowed to recover for 2–4 h. For the recording sessions, mice were placed in the head-plate holder above the free-floating ball and allowed to habituate for 5-10 minutes. The agarose and silicone plug were removed, the well was covered with warm sterile saline and the reference insulated silver wire electrode (A-M Systems, Carlsborg, WA) was placed in cerebellum. A multisite electrode spanning all cortical layers (A1x16-5mm-50-177-A16; Neuronexus Technologies, Ann Arbor, MI) was coated with DiI (Invitrogen) to allow post hoc insertion site verification and then inserted in the brain through the craniotomy. The electrode was lowered until the uppermost recording site had entered the brain and allowed to settle for 20-30 minutes, after which the ipsilateral eye response was checked to confirm the proper location in V1. The well with the electrode was then filled with 3% agarose to stabilize the electrode and the whole region was kept moist with surgical gelfoam soaked in sterile saline (Pfizer, MA). Minimum 2 penetrations were made per animal to ensure proper sampling of the craniotomy. For Figure 7, only one penetration per recording was made, at identical sites in the center of cranitomy (location was measured by micromanipulator using edges of the craniotomy as a reference point). Recordings sessions typically lasted 2-3 h. After the recording, mice were euthanized with an overdose of ketamine and xylazine. The brains were then isolated and fixed in 4% PFA overnight at 4°C. Brains were subsequently sectioned at 100 μm using a vibrating microtome. The sections were incubated in DAPI (Sigma), floated on slides and mounted in Aquamount. The sections were imaged on a Keyence microscope as described above to confirm the electrode location within bV1.

Visual stimuli, data collection and analysis

Visual stimuli were generated with MATLAB (MathWorks, Natick, MA) using the Psychtoolbox extension (Brainard, 1997) and Spike2 (CED, Cambridge, UK). Varying frequencies and orientations of full-field sinusoidal gratings at 100% contrast were displayed on a gamma corrected 17" LCD (Niell and Stryker, 2008) for 1.5 s with 0.2 s interstimulus interval (gray screen). Stimuli were presented in randomized fashion and each stimulus was presented 30-50 times on average during a recording session. The screen was centered 20 cm from the mouse's eye, covering ~80° of visual space. 30-50 light-emitting diode (LED) flashes were presented before or after the sinusoidal gratings with 10 s interstimulus interval. Non-stimulated eye was covered with custom-made blocker. Visual response signals were preamplified 10x (MPA8I preamplifiers; Multi Channel Systems MCS GmbH, Reutlingen, Germany) and then fed into a 16-channel amplifier (Model 3500; A-M Systems), amplified 200x and band-pass filtered 0.3-5000 Hz. The signals were sampled at 25 kHz using Spike2 and data acquisition unit (Power 1401-3, CED). Stationary and movement stages of animal behavior were separated using an optical mouse that tracked the movement of the styrofoam ball and was interfaced with LabView (Austin, TX) and Spike2, or using video recordings timed to stimuli presentation (WansView, Shenzhen, PRC). Only stationary, non-running stages were analyzed offline using Spike2 software (CED). LFPs were analyzed as waveform averages, triggered by stimulus onset. Visually evoked potentials (VEPs) were defined as negative-going events occurring within 200 ms following stimulus onset, having an amplitude of more than 3x standard deviation and having a width at half maximum of less than 50 ms (Li et al., 2013). For estimation of C/I ratio, VEP amplitude evoked by sinusoidal gratings at 0.15 cycles per degree (cpd) was combined with amplitudes evoked by LED as they were identical in nature. For acuity analysis, responses from 4 different frequencies from all orientations ranging from 0.05-0.6 cpd were plotted on a logarithmic scale and acuity was estimated from linear regression as the frequency where amplitude equals 0 (Porciatti et al., 1999). For multi-unit analysis, spikes were extracted from band-pass filtered data using thresholds (3x standard deviation) and sorted in Spike2. Peri-stimulus time histogram (PSTH) analysis was performed with Spike2 using 0.01 s bins. Spontaneous firing was calculated as average firing rate before stimulus presentation with 0.2 s offset. Spontaneous firing was subtracted from peak poststimulus firing rate to determine evoked firing rate. For analysis of single units, spikes were isolated using template matching and principal component analysis in Spike2. PSTHs were calculated using 0.001 s bins with 0.2 s offset, using

0-180° (−90° to 90°) orientations in 30° increments at 0.15-0.6 cpd as stimulus. Responses were plotted over all orientations and preferred orientation was determined ad the orientation where maximum spiking occurred after fitting a Gaussian curve. Orientation selectivity index (OSI) was calculated as the ratio of (Rpref – Rorth)/(Rpref + Rorth), where Rpref is the firing rate at preferred orientation and Rorth at orientation orthogonal to preferred. Cells with OSI > 0.3 were included in the analysis. Orientation difference (ΔO) of single units was calculated as the difference of preferred orientations between responses to contra and ipsi eye stimulation (Wang et al., 2010). Spectral analysis was performed on raw LFP traces as previously described (Mohns and Blumberg, 2008), with gamma-band oscillations defined as 40-70 Hz, as described in (Chen et al., 2015). Data collection and analyses were performed blind to genotype or experimental group.

QUANTIFICATION AND STATISTICAL ANALYSIS

All quantitated analyses were performed with the researcher blind to the condition, as stated above. Statistical analyses were performed in SigmaPlot 11 and 13 (San Jose, CA) or GraphPad Prism 7.0 (GraphPad Inc., La Jolla, USA) using t test and one or two-way repeated-measures or regular ANOVA with post hoc comparisons (as indicated in text, figure legends and Supplementary Tables), unless stated otherwise. When comparing two independent groups, normally distributed data were analyzed using a Student's t test. In the case data were not normally distributed a Mann-Whitney rank sum test was used. All data are reported as mean ± SEM, where N represents number of animals used, unless indicated otherwise. Target power for all sample sizes was 0.8. In all cases, alpha was set to 0.05.

DATA AND SOFTWARE AVAILABILITY

Mendeley Data repository containing all original representative images can be found under the following link: https://doi.org/10.17632/9wdt9rvhck.2.